Revision 2

Word count: 9736

# $Fe^{3+}/Fe^{T}$ ratios of amphiboles determined by high-spatial resolution single-crystal synchrotron Mössbauer spectroscopy

**Barbara C. Ratschbacher[1,2], Jennifer M. Jackson[1], Thomas S. Toellner[3], Claire E. Bucholz[1], Wolfgang Sturhahn[1], Natalia V. Solomatova[4]**

*[1]Division of Earth and Planetary Sciences, California Institute of Technology, 1200 E. California Blvd., Pasadena, California, 91125, U.S.A.*

*[2]Department of Earth and Planetary Sciences, University of California, Davis, One Shields Avenue, Davis, California, 95616, U.S.A.*

*[3]Argonne National Laboratory, 9700 South Cass Avenue, Argonne, IL 60439, USA.*

*[4]Laboratoire de Géologie de Lyon, École Normale Supérieure de Lyon, CNRS UMR 5276, 46 Allée d'Italie, Lyon, 69364, France*

## Abstract

The $Fe^{3+}/Fe^{T}$ ratios ($Fe^{3+}/[Fe^{2+} + Fe^{3+}]$) in minerals can be used to understand their crystallization and post-crystallization conditions. However, as natural minerals are often zoned and contain inclusions, bulk techniques, e.g., wet chemistry, may not provide

accurate $Fe^{3+}/Fe^{T}$ values for a single phase of interest. We determined $Fe^{3+}/Fe^{T}$ ratios of amphiboles along different crystallographic orientations by single-crystal synchrotron Mössbauer spectroscopy (SMS) in energy and time domain modes from four volcanic localities (Long Valley Caldera, Mt. St. Helens, Lassen Volcanic Center, USA and Mt. Pinatubo, Philippines). The high spatial resolution (as low as $12 \times 12$ μm spot size) and standard-free nature of SMS allow the detection of intra-grain compositional heterogeneities in $Fe^{3+}/Fe^{T}$ with relatively low uncertainties.

We combine SMS with major element compositions, water contents, and hydrogen isotope compositions to document the $Fe^{3+}/Fe^{T}$ ratios as a function of mineral composition and post-crystallization dehydrogenation. Spectra were fitted with up to five distinct sites: ferrous iron on M(1), M(2), M(3), and ferric iron on M(2) and M(3), consistent with x-ray diffraction studies on single crystals of amphibole. The $Fe^{3+}/Fe^{T}$ ratios range from 0.14 ± 0.03 (Long Valley Caldera), 0.51 to 0.63 ± 0.02 (representing intra-grain heterogeneities, Mt. St. Helens) to 0.86 ± 0.03 (Lassen Volcanic Center). The latter grain experienced post-crystallization dehydrogenation evidenced by its low water content (0.6 ± 0.05 wt%) and its elevated hydrogen isotope composition ($\delta$D = +25 ± 3 ‰ relative to SMOW). The $Fe^{3+}/Fe^{T}$ ratios of 0.62 ± 0.01 and 0.20 ± 0.01 of two Mt. Pinatubo grains correlate with high-$Al_2O_3$ cores, and low-$Al_2O_3$ rims and smaller phenocrysts in the sample, respectively. This study shows that SMS is capable to distinguish two different domains with dissimilar $Fe^{3+}/Fe^{T}$ values formed under different crystallization conditions, demonstrating that SMS in combination with major element, water, and hydrogen isotope compositions allows the interpretation of amphibole $Fe^{3+}/Fe^{T}$ ratios in the context of crystallization and post-crystallization processes.

**Keywords:** amphibole, Mössbauer spectroscopy, $Fe^{3+}/Fe^{T}$ ratios, dehydrogenation

## Introduction

Amphiboles are common minerals in hydrous mafic to felsic arc magmas (e.g., Hawthorne and Oberti 2007; Krawczynski et al. 2012). Due to their common occurrence and stability over a wide pressure, temperature, and compositional range, the chemistry of amphiboles has been used to infer processes such as magma mixing and recharge (e.g., Kiss et al. 2014; Barnes et al. 2016; Zou and Ma 2020) and to reconstruct the pressure and temperature histories of volcanic and plutonic rocks (e.g., Humphreys et al. 2019; Peters et al. 2017; Mutch et al. 2016; Johnson and Rutherford 1989).

Amphiboles incorporate both ferrous ($Fe^{2+}$) and ferric iron ($Fe^{3+}$) into their crystal structure. Thus, the $Fe^{3+}/Fe^{T}$ ratio has the potential to record the oxygen fugacity of the melt from which they crystallized (e.g., King et al. 2000). However, the use of $Fe^{3+}/Fe^{T}$ ratios in natural amphiboles as potential indicatiors of magma chemistry requires their accurate determination. Bulk techniques such as wet chemistry and conventional Mössbauer spectroscopy suffer from potentially averaging intra-grain compositional variability and inclusions occurring in natural amphiboles, thus posing a challenge to accurately reflect the conditions during amphibole crystallization. A high spatial resolution technique with low uncertainties is required to understand amphibole $Fe^{3+}/Fe^{T}$ ratios in the context of their magmatic history.

We characterize volcanic amphiboles by single-crystal synchrotron Mössbauer spectroscopy, an analytical technique that provides the spatial resolution to avoid

averaging heterogeneous grains and to detect intra-grain $Fe^{3+}/Fe^{T}$ ratio variations. Furthermore, it uses the physics of nuclear forward scattering on single-crystals (e.g., Sturhahn and Gerdau 1994; Sturhahn 2000, 2004) and therefore does not require reference spectra for data interpretation as required for other techniques determining $Fe^{3+}/Fe^{T}$ ratios (e.g., X-ray absorption near edge structure spectroscopy; Dyar et al. 2016). Moreover, synchrotron-based Mössbauer spectroscopy is time-efficient compared to conventional Mössbauer spectroscopy. Herein, we investigate calcic amphiboles from four volcanic localities. We determine their major and minor element composition (electron microprobe), water content and hydrogen isotope composition (secondary-ion mass spectrometry), unit cell parameters (X-ray diffraction), and $Fe^{3+}/Fe^{T}$ ratios, using time- and energy-domain synchrotron-based Mössbauer spectroscopy at the Advanced Photon Source at Argonne National Laboratory, USA. We discuss our results in the context of amphibole mineral chemistry as well as crystallization and post-crystallization processes.

## Samples

Four volcanic samples were selected for this study. Sample MC18-2 is from a lava flow sampled at the West Moat coulee (age 161 ± 2 ka; Hildreth 2004) in the Long Valley Caldera (California, USA) and thus part of the post-caldera rhyolitic flows following the Bishop tuff eruption (~760 ka), which created the Long Valley Caldera (e.g., Hildreth and Mahood, 1986; Crowley et al. 2007). Sample LF02-042 is from a lava flow from the Kings Creek sequence (Underwood et al. 2012) of the Lassen Volcanic Center (LVC) in northern California. The LVC marks the southernmost part of the

Cascades arc; the Lassen Domefield represents the final stage of the LVC and contains ~35 ka biotite- and hornblende-bearing rhyodacites located in the Kings Creek and Hat Creek areas east of Lassen Peak (e.g., Turrin et al. 1998; Clynne and Muffler 2010). Sample SH315-4 was collected from a dacite lava spine ejected during the 2004 to 2006 crystal-rich and gas-poor eruption at Mt. St. Helens (USA; e.g., Pallister et al. 2008; Thornber et al. 2008). Sample PH13A (two grains analyzed from this sample) is a phenocryst-poor dacite pumice erupted as part of the cataclysmic eruption in June 1991 at Mt. Pinatubo, a prominent stratovolcano in the Bataan segment of the Taiwan-Luzon arc in the Philippines (e.g., Pallister et al. 1996).

## Methodology

### Sample preparation

Amphiboles were separated using a jaw crusher and a Frantz Isodynamic Magnetic Separator. Individual grains were crushed to <700 μm, handpicked under a binocular microscope, mounted in epoxy, and polished for analysis by electron microprobe (EMPA) and secondary-ion mass spectrometry (SIMS). Most grains are fragments of whole grains to maximize the total integrated intensities, while avoiding thickness effects. Analyses of thinner grains are possible but require longer data collection times, especially if samples are not enriched in $^{57}$Fe. Based on backscatter electron images and chemical compositions, we selected grains with the fewest inclusions, and alteration and/or decomposition features. One grain was selected from each sample, except for sample PH13A, from which we selected two grains (PH13A A1 and PH13A A2). After EMPA and SIMS analysis, we removed the grains from the epoxy

and glued them on a micromesh for single-crystal X-ray diffraction (XRD) analysis. Finally, the grains were glued with a known orientation on a Plexiglas slide for SMS analyses. After SMS analyses, grain PH13A A1 was removed from the Plexiglas slide and pressed in indium for a second set of water analyses by SIMS. Grain PH13A A2 is the only grain which has been analyzed by SIMS only after SMS analyses. The details of each of these steps are described below.

**Electron microprobe analysis**

Major and minor elements in amphibole were determined using a JEOL JXA-8200 electron microprobe at the California Institute of Technology after each grain was imaged in electron backscatter mode. Multiple points (transects through entire grains) were analyzed on each individual grain to map intra-grain compositional variations. We used an acceleration voltage of 15 kV, a beam current of 25 nA, and a defocused beam of 10 μm diameter, analyzing Si, Al, Mg, Ca, Na, K, Fe, Mn, Ti, F, and Cl with counting times set to 20 seconds for each element and 10 seconds for the background. The following standards were used to calibrate the elemental peaks prior to analyzing the unknowns: forsterite, Shankland P-658 (Mg), fayalite RDS P-1086 (Fe), Mn olivine RDS P-1087 (Mn), synthetic anorthite (Si, Al, Ca), Amelia albite (Na), Asbestos microcline (K), synthetic $TiO_2$ (Ti), synthetic $Cr_2O_3$ (Cr), synthetic F-phlogopite (F), and synthetic sodalite (Cl). Data reduction was performed by a modified ZAF procedure (CITZAF; Armstrong 1995). The detection limits were ≤0.01 wt% for $SiO_2$, $Al_2O_3$, MgO, $TiO_2$, CaO, $K_2O$, and Cl; ≤0.02 wt% for FeO, $Na_2O$, $Cr_2O_3$, MnO, and F. The EMPA analysis

results and their 1σ uncertainties (percent of absolute values) calculated from counting statistics are listed in Supplementary Table 1.

**Secondary-ion mass spectrometry**

Water concentrations and D/H ratios were obtained on a Cameca 7f-GEO SIMS at the California Institute of Technology where such analysis of $H_2O$ and D/H ratios are routinely performed on nominally anhydrous minerals (olivine, pyroxene, plagioclase; Mosenfelder et al. 2011; Chin et al. 2016), apatite (e.g., Boyce et al. 2010; Treiman et al. 2016), melt inclusions (Taylor et al. 2016; Ni et al. 2017) with well-established analytical protocols. We developed a new but similar protocol for our amphiboles. Two natural amphiboles (magnesio-hastingsite from Kipawa, Canada; $H_2O$: 1.45 ± 0.19 wt%; δD: -88 ± 10‰ (relative to SMOW), and a magnesio-arfvedsonite from Ilìmaussaq, Greenland: $H_2O$: 1.45 ± 0.12 wt%; δD: -142 ± 10‰), previously characterized for their water contents and D/H ratios by Deloule et al. (1991), were used as reference materials. Anhydrous olivine from the Springwater meteorite served to determine background $H_2O$. The latter can reach ≤1 ppm for epoxy-free sample mounts; ~10 ppm for polished thin sections; and tens to hundreds ppm for epoxy mounts. Although we mounted our amphiboles in epoxy, the high $H_2O$ concentrations in our amphiboles made the background corrections insignificant. In addition, the sample mounts were kept for >48 h at $10^{-9}$ torr in the sample chamber prior to analysis to reduce the background signal. For the $H_2O$ analysis, a focused, 10 keV $Cs^+$ primary beam of 4-5 nA (~15 μm in diameter) was used to pre-sputter the sample in rastering (10 × 10 μm) mode for 120 seconds. The raster size was reduced to 5 × 5 μm during sample data acquisition. $^{12}C$, $^{17}O/^{1}H$, and

$^{18}O/^{1}H$ were sequentially measured on an electron multiplier in the peak-jumping mode for 20 cycles, with 1 second counting times for each mass. We used a mass resolving power (MRP) of 5500 to remove the $^{17}O$ interference from $^{18}O/^{1}H$. The hydrogen isotope analyses were performed after the $H_2O$ analyses in the same area of the sample, with similar beam conditions. Because of the low $^{2}H^{-}$ counting rate, a large field aperture (300 μm) was used. Secondary ions ($^{1}H^{-}$, $^{2}H^{-}$) were collected using a MRP of 500 for 20 cycles on the samples and 40 cycles on the reference materials. In each cycle, the counting times were 1 second for $^{1}H^{-}$ and 8 seconds for $^{2}H^{-}$. Typical $\sigma_{mean}$ uncertainties (percent of absolute values) were at ~8 % for water concentrations and include the counting statistical error of each point and the propagated error from the calibration line determined from the standards. For hydrogen isotopic measurements, the errors of the δD values include the counting statistical error of each individual measurement and the standard deviation of repeated analysis of the standards. The measurements (including counts, uncorrected and corrected data) are listed in Supplementary Table 1.

**Single-crystal X-ray diffraction**

We conducted single-crystal X-ray diffraction experiments at the X-Ray Crystallography Facility in the Beckman Institute at the California Institute of Technology, using either a Bruker AXS D8 VENTURE four-circle diffractometer with Molybdenum or Copper Kα radiation from a IμS microsource or a Bruker AXS KAPPA APEXII four-circle diffractometer using Molybdenum Kα radiation from a sealed-tube X-ray generator. The XRD datasets represent coverage of reciprocal space in between that needed for a typical orientation matrix and a full crystal structure refinement. The

latter is required to solve for atomic positions and exclude the presence of micro-twinning but requires a sample at most 100 μm in size to minimize the amount of crystal in the beam. This is much smaller than the several hundred micron grains selected for our study. A large grain size was preferred to analyze potential $Fe^{3+}$ heterogeneity within single amphibole grains using SMS. Therefore, we cannot rule out the presence of micro-twinning in some of our grains.

The APEX3 software (Bruker 2012a) was used for fitting diffraction peaks and refining lattice parameters. In addition, we used the CELL_NOW program (Bruker 2012b) to index the unit cell. In-situ video collection was used to identify crystal faces for each grain. All experiments were conducted at room temperature.

The collection of XRD data had three goals: (a) to determine the unit cell parameters and correlate them with $Fe^{3+}/Fe^{T}$ ratios; (b) to exclude crystals which reveal large-domain twinning and/or contain inclusions; (c) index crystal faces to control the orientation of the X-ray propagation and polarization directions relative to the crystallographic axes of the single crystal during SMS measurements. Each grain was glued onto a Plexiglas slide in a known orientation for SMS analyses. The Plexiglas could then be rotated relative to the X-ray propagation and polarization directions to analyze different orientations (Fig. 1).

**Single-crystal synchrotron Mössbauer spectroscopy**

Mössbauer spectroscopy (MS) yields information on the valence state, local bonding, and magnetism of $^{57}Fe$ in a solid through hyperfine interactions of the Fe nucleus with its environment and their influence on the absorption and re-emission of

gamma rays (e.g., Margulies and Ehrman 1961; Sturhahn and Gerdau 1994; Fultz 2002; Sturhahn 2004, 2005; Dyar et al. 2006; Sturhahn and Jackson 2007; Vandenberghe and Grave, 2013). It is worth noting the advantages of time-resolved synchrotron Mössbauer spectroscopy. For example, the brightness of the source for SMS is very high (~$10^{23}$ photons/sec/eV/sr), compared with radioactive sources used for conventional Mössbauer spectroscopy (100 mCi $^{57}$Co source: ~$10^{13}$ photons/sec/eV/sr). The signal to noise ratio (S/N, or quality) of SMS spectra is also very high. The SMS measurements of the amphibole samples reported here produce very high signal to noise ratio spectra (~$10^{3}$:1, for amphiboles with counting rates ~20 to 30 Hz and a detector background level measured at ~0.02 Hz), compared with radioactive sources used for conventional Mössbauer spectroscopy (~$10^{-2}$:1 for 100 mCi $^{57}$Co source) (e.g., Sturhahn 2004). The quality of the spectra can be understood based upon the information content in a given spectrum. The very low S/N value for conventional Mössbauer spectroscopy can be understood based upon determining the total area of the absorption peaks (resonant signal originating from the sample) and comparing it with the total area of the spectrum. Note that wider velocity-ranges lead to lower S/N. That is, a significant fraction of the data acquired in such a measurement is non-resonant, i.e., background. In an SMS measurement, every photon detected is a signal. The S/N for SMS is high not necessarily because the counting rates are so high, rather the background is extremely low.

For single crystals, the collection of synchrotron Mössbauer time spectra along distinct crystallographic orientations (Fig. 1) yields additional constraints due to the linear polarized nature of synchrotron radiation and the inherent polarization dependence of the hyperfine interactions. This sample-orientation dependence in single-crystal time

spectra helps to disentangle and identify contributions from numerous crystallographically distinct ferric and ferrous $^{57}$Fe sites in amphiboles. More discussion on the comparison between time- and energy-domain Mössbauer spectroscopy can be found in Sturhahn (2004) and references therein.

SMS measurements were performed at beamline 3ID of the Advanced Photon Source at Argonne National Laboratory. Three different measurement setups were used to collect SMS spectra of amphibole single crystals. These setups uniquely allow us to arrive at the best possible model of hyperfine parameters for these amphibole grains by collecting spectra 1) in the time- and energy-domain using the linear polarized nature and very high brightness of a synchrotron radiation source and 2) in the time-domain with delay times up to ~450 ns, and 3) with an efficient use of beamtime. These setups operate with different filling patterns in the storage ring (24-bunch mode and hybrid mode) and different x-ray optics to provide a stable beam of 14.4 keV photons. Time calibration was performed for each set of measurements. The setups are described here.

**(1) 24-bunch mode setup.** These measurements were performed at station B at beamline 3ID using a setup similar to previous studies (e.g., Solomatova et al. 2019; Fig. 2a). Synchrotron radiation from the beamline's undulator has its bandwidth reduced to 2eV (full width at half maximum, FWHM) centered at 14.413 keV using a LN2-cooled silicon double-crystal monochromator. A secondary, high-resolution monochromator reduces the bandwidth further to 1meV (FWHM) (Toellner 2000). X-rays were then focused on the sample to a spot size of 20 x 20 μm$^2$. An optical microscope allowed the positioning of the X-

ray beam on approximately the same spot used for the EMPA and SIMS measurements. An avalanche photodiode detector and conventional time-filtering electronics were used to collect time spectra in the forward direction between delay times of around 22 to 120 ns, dependent on storage ring filling quality. The incident beam power density (flux density) on the sample was $1.7 \times 10^7$ ph/s/μm$^2$. The collection time for one orientation varied between 1 to 3 hours, dependent on the grain thickness, the Fe content, and the hyperfine fields.

**(2) Hybrid mode setup using high-speed shutters: Time-domain.** These measurements were performed at station D at beamline 3ID using a new spectrometer (Toellner et al. in preparation; Toellner et al. 2011) that implements a pair of high-speed shutters to extract the SMS signal using the single bunch of the hybrid mode as the excitation pulse (Fig. 2b). It operates without a high-resolution monochromator. The beam was focused on the sample with a spot size of $12 \times 12$ μm with a flux density of $1.0 \times 10^{10}$ ph/s/μm$^2$. The spectra measured in this mode have an accessible time window that is significantly longer compared to the 24-bunch mode, but begins at delay times of >60 ns. Despite the capability of measuring long delay times, our samples typically produced little signal beyond approximately 210-450 ns. In addition, this dual-shutter setup achieves higher counting rates than during the 24-bunch mode, which significantly reduces measurement time and is an advantage for samples with low amounts of $^{57}$Fe.

**(3) Hybrid mode setup using high-speed shutters: Energy-domain.** The setup is similar to the hybrid mode time-domain setup described above, but includes a Mössbauer drive (with a single-line resonant material), inserted between the microfocusing optics and shutter 1 (Fig. 2b). A 10 μm-thick 304-grade stainless steel foil (natural abundance of $^{57}$Fe) was used as the single-line emitter. An absorption spectrum of the sample convolved with that of the single-line emitter was measured by collecting the radiation transmitted through the sample as a function of the velocity, or Doppler shift, of the Mössbauer drive. The velocity calibration of the drive was performed using the known spectrum of an α-Fe foil. The scan range of the two collected energy-domain spectra varied between +4 to -4 mm/s and +6 to -6 mm/s. Spectra were collected for 12 hours each with a spot size of 12 × 12 μm.

**Data collection procedures.** For each amphibole grain, we collected time spectra with and without a well-characterized stainless steel (SS) reference foil (natural isotopic distribution of $^{57}$Fe; thickness of 5 or 10 μm). Collection times are a function of Fe content and sample thickness; for grain-only they are between ~1 to 3 hours and ~1 hour for the grain with the SS reference foil. The foil was secured and placed in the upstream direction as a reference absorber to determine the isomer shift, which is strongly sensitive to the oxidation state of iron. A time spectrum of a grain was always followed by a spectrum of the grain with SS foil. In the 24-bunch mode setup, we collected up to three sets of spectra with delay time windows of about 22 to 120 ns for different crystallographic orientations (Fig. 1). We specify crystal orientations in terms of: 1) the

298 lattice planes (*hkl*) that were oriented perpendicular to the incident X-ray beam during the
299 SMS measurements and therefore perpendicular to the X-ray propagation vector, and 2)
300 the direction of polarization. For grains MC18-2, SH315-4, and PH13A-A2, we placed an
301 aperture on the grain to ensure fiducial placement of the x-rays. The aperture is a Cu strip
302 with a ~100 μm diameter opening drilled into it using an electric discharge machine,
303 which facilitates locating the center of the aperture by scanning across its width,
304 guaranteeing that exactly the same spot was analyzed for the first and second
305 orientations. For grains LF02-042 and PH13A A1, no aperture was used, but data were
306 also collected in a third crystallographic orientation (Fig. 1). Supplementary File 1 lists
307 the number of spectra and collection time for each sample for different orientations and
308 with different modes. On grain SH315-4, data from two additional areas were collected to
309 evaluate intra-grain compositional heterogeneity.
310 In hybrid mode, time spectra with delay times ranging from 60 to 350 ns (one-
311 hour collection time) and 100 to 500 ns (overnight collection time) were measured for at
312 least one crystallographic orientation. For grains MC18-2 and SH315-4, energy domain
313 spectra were also collected.
314

315 **Crystal chemistry of iron in amphiboles**

316 The amphibole formula can be written as $AB_2C_5T_8O_{22}W_2$ (Hawthorne and Oberti
317 2007) with A, B, C, and T referring to groups of cations occupying specific sites in the
318 structure. There are three distinct octahedrally coordinated M sites that are occupied by C
319 cations, M(1), M(2), and M(3), and one site, M(4), that is occupied by B cations.
320 Amphiboles incorporate $Fe^{2+}$ and $Fe^{3+}$ only in octahedral coordination (B and C cations).

Iron in tetrahedral coordination (T cations) has not been documented (Hawthorne and Oberti 2007). Few studies performed conventional MB spectroscopy and a complete structural refinement from single-crystal XRD data on amphiboles (e.g., Redhammer and Roth 2002; Driscall et al. 2005; Abdu and Hawthorne 2009; Uvarova et al. 2007; Oberti et al. 2018). These studies provide information about site preferences of $Fe^{2+}$ and $Fe^{3+}$: $Fe^{3+}$ strongly prefers the M(2) site whereas $Fe^{2+}$ dominates the M(1) and M(3) sites but can also occur on the M(4) site. The preference for $Fe^{2+}$ is M(1)>M(3)>>M(2), although Oberti et al. (2007) documented a random distribution between the M(1) and M(3) sites for amphiboles crystallized at high temperatures. In calcic amphiboles, $Fe^{2+}$ may occupy the M(4) site (e.g., Goldman and Rossman 1977), but as discussed below, a $Fe^{2+}$ M(4) site is not necessary to achieve a good fit for the SMS spectra in this study. Ferric iron only occurs on the M(2) site in amphibole with a fully occupied W = $(F, Cl, OH)_2$ site but can occur at M(1), M(2), and M(3) in amphiboles with an oxo-component (O at the W-site in addition to F, Cl, and OH; Oberti et al. 2007). The oxidation of $Fe^{2+}$ to $Fe^{3+}$ on the M(1) and M(3) sites is the major mechanism to achieve local bond-valence satisfaction during loss of hydrogen from the structure and the formation of the oxo-component (dehydrogenation; e.g., Oberti et al. 2007; Della Ventura et al. 2018).

**Defining the Mössbauer sites and spectral fitting**

**Computing the Euler angles.** We define six distinct Mössbauer sites (MB sites) corresponding to the M(1), M(2), M(3) sites, which can be each occupied by $Fe^{3+}$ and/or $Fe^{2+}$. These are as follows: $Fe^{2+}$ on M(1); $Fe^{2+}$ on M(2); $Fe^{2+}$ on M(3); $Fe^{3+}$ on M(1); $Fe^{3+}$

343 on M(2); $Fe^{3+}$ on M(3) . We note that introducing a $Fe^{2+}$ M(4) site in our model does not
344 improve the fitting of our spectra (see result section).

345 For each of the M(1), M(2), M(3) sites, which can be occupied by $Fe^{2+}$ and/or
346 $Fe^{3+}$, unique Euler angles, describing the orientation of the electric field gradient at the
347 $^{57}Fe$ nucleus with respect to the orientation of the single crystal, can be calculated. By
348 calculating Euler angles for each MB site (see below), we clearly define and relate each
349 MB site to a crystallographic site via atomic parameters. Thus, each site's contribution to
350 the overall spectrum is distinguishable. We used published atomic parameters of each site
351 (MB and non-MB sites; Supplementary Table 2) of a magnesio-hornblende amphibole
352 with a similar major element composition as our amphiboles (Makino and Tomita 1989).
353 We combined these parameters with unit cell base vectors and angles from the XRD
354 analyses and the EMPA data, from which we can allocate cations and anions to
355 crystallographic sites to define each site and its cation and or anion occupation. The kvzz
356 executable in the CONUSS (Coherent nuclear resonant scattering by single crystals)
357 software package (Sturhahn 2000; www.nrixs.com) allows calculating the main axes of
358 the electric field gradient from the local symmetry around the iron nucleus and thus the
359 calculation of the Euler angles. The kvzz executable requires defining each MB and non-
360 MB site not only by the atomic parameters but also by its occupation and site weight. For
361 example: there are five C cations in the amphibole structure: Ti, Al, Mn, Fe, Mg; grain
362 SH315-4 has 2.03 apfu Fe on the C sites and shares these with 0.09 apfu Ti, 0.41 apfu Al,
363 and 2.47 apfu Mg (adding up to 5 apfu); thus, the total Fe-site weight is 0.40. There are
364 six distinct MB sites, three $Fe^{2+}$and three $Fe^{3+}$ sites corresponding to M(1), M(2), and
365 M(3), thus each MB site has a site weight of 0.07. Amphibole grains vary in major

element compositions, which influences site weights, average bond lengths, and unit cell parameters, and therefore the Euler angles. However, these variations have a minimal effect on the calculated angles; for example, variations of 0.5 apfu Fe on the C sites and a ≤0.1 Å difference between unit cell base vectors only change the Euler angles by <0.132°. The Euler angles are listed in Supplementary Table 3.

**Establishing a starting model for spectral fitting.** Conventional MB studies also provide information about the range of hyperfine parameters of $Fe^{2+}$ and $Fe^{3+}$. We compiled hyperfine parameters from conventional MB studies on amphiboles and use these as a guide to constrain our fitting models (see Supplementary File 4 for data and references). In general, $Fe^{3+}$ shows quadrupole splitting (QS) between 0.25 to 1.70 mm/s compared to 1.19 to 2.93 mm/s for $Fe^{2+}$ (Supplementary Table 4). The isomer shift (IS; with respect to $\alpha$-Fe) for $Fe^{3+}$ is close to 0.4 mm/s (Supplementary Table 4). The IS for $Fe^{2+}$ is between 0.97 to 1.28 mm/s (Supplementary Table 4). All studies report that the $Fe^{3+}$ M(3) site has higher QS than the other $Fe^{3+}$ sites. Similarly, the $Fe^{2+}$ M(1) site has higher QS than the other $Fe^{2+}$ sites. However, conventional MB spectroscopy proves challenging to ascribe $Fe^{3+}$ and $Fe^{2+}$ to specific crystallographic sites. Therefore, we do not let our models be constrained by these values; rather we use these ranges as guidelines for a starting model to fit our data.

**Fitting the data.** We fitted our SMS spectra using version 2.2.1 of the CONUSS software package (Sturhahn 2021). All fitted spectra incorporate the transmission integral (Margulies and Ehrman 1961; Sturhahn and Gerdau 1994). We used the dual fit module,

which allows simultaneous fittings of data with and without the reference SS foil. We aimed to develop a single-crystal chemical model in CONUSS that best fits all individual spectra of each grain.

The recoil-free fraction, also known as the Lamb-Mössbauer factor $f_{LM}$, is used to fit the data in the CONUSS software package. We used an estimated, but reasonable value of the Lamb-Mössbauer factor of 0.75 to fit our amphibole data. Highly accurate values of the average $f_{LM}$ can be obtained, for example, by conducting nuclear resonant inelastic x-ray scattering measurements (NRIXS) on the phase of interest (e.g., Murphy et al. 2013; Morrison et al. 2019; Ohira et al. 2021) or on materials that have similar valence and coordination environments and are at similar PT conditions. High-statistical quality NRIXS measurements on unenriched samples like the amphiboles studied here require several days (to a week or more), as we would need to isolate the much smaller zone-free region of the grains. Our estimated value of 0.75 is reasonable considering values determined for minerals containing octahedrally coordinated ferrous (enstatite: $0.709\pm0.003$ for $En_{80}$ to $0.723\pm0.003$ for $En_{93}$, Jackson et al. 2009) and octahedrally coordinated ferric iron in hydrous minerals (goethite: 0.77, Dauphas et al. 2012; uncertainties were not provided). If one assumes these cited end-member values given here, the resulting effect on the $Fe^{3+}/Fe^{T}$ ratio is within the cited uncertainties.

CONUSS was also used to pre-determine the optimal grain thickness before multiple-scattering effects dominate the measured spectrum. This guided our selection of suitable grains for SMS analysis. The kfor executable computes the local effective thickness and Supplementary Table 3 lists the local effective thicknesses for the various

411 datasets. Except for the third orientation of grains LF02-042 and PH13A A1, all values
412 are <1, thus thickness effects are not expected.

413 For data fitting, we use the kmco executable in CONUSS, which entails a Monte
414 Carlo sampling approach to explore the parameter space. This has been done within the
415 starting model parameter range (see section above) as well as outside these ranges to
416 explore whether better fits can be achieved. Refinements of fits have been carried out
417 using the kctl executable in CONUSS.

418 Imperfect alignment of the grain's principle crystallographic axes with the x-ray
419 propagation direction as a result of minimal tilting of the grain during mounting on the
420 plexiglass slide causes a deviation in the canting angle from 0° in orientations 1 and 3
421 and 90° in orientation 2 (Fig. 1). Fitting of the canting angle resulted in a maximum
422 deviation of 23° from the expected values and can be explained by this misalignment.

423 The presence of fractures and/or strain in our crystals, potentially acquired during
424 eruption, as well as twinning have an impact on the texture coefficient. A texture
425 coefficient of 100% is expected for perfect single crystals, indicating no randomly
426 orientated hyperfine fields. The presence of micro-twinning, impossible to detect from
427 the limited "orientation matrix" XRD data we collected, can account for a texture
428 coefficient below 100%. Thus, in a final step of fitting, we varied the texture coefficient,
429 which led to improved consistency of fits for the different orientations. Different texture
430 coefficients would be expected for different orientations (24-bunch mode data; Fig. 1) as
431 the orientation of the micro-twin(s) with respect to the larger grain is difficult to
432 constrain. Imperfect alignment of the grain (discussed above) can also partly explain a
433 texture coefficient below 100%.

## Results

### Amphibole major element compositions, water content, and δD

Amphibole colors observed in thin section range from green-brown to yellow-red. A red color in volcanic amphiboles was attributed to post-crystallization iron oxidation during eruption and cooling via $H_2$ loss (i.e. dehydrogenation; e.g., Dyar et al. 1993; Miyagi et al. 1998). LF02-042 shows a red color, whereas grains MC18-2, SH315-4, PH13A A1, and PH13A A2 have no reddish color (Supplementary Figure 1 shows thin section images of each sample).

The amphiboles examined here are calcic amphiboles (nomenclature after Hawthorne et al. 2012 shown in Fig. 3a). Grain MC18-2 contains inclusions of feldspar, magnetite, and apatite (Fig. 4a); LF02-042 and PH13A A2 have no inclusions at the surface (Fig. 4b, e); SH315-4 has magnetite inclusions and is discolored along fractures and around inclusions (Fig. 4c); PH13A A1 includes magnetite at its edges (Fig. 4d).

FeO contents in amphiboles are ~20 wt% (MC18-2), ~18 wt% (SH315-4), ~13 wt% (PH13A A2), and ~12 wt% (LF02-042; Fig. 4). Grain PH13A A1 shows intra-grain compositional variability: $Al_2O_3$ decreases from 12 wt% in the interior (brighter area in the BSE image) to 7-8 wt% in the rim (darker area; Fig. 4d). CaO also decreases from the core (12 wt%) to rim (8-9 wt%). FeO decreases from 13 wt% at spot 1 to 10 wt% at spot 12 (Fig. 4d). The intra-grain variability in the other grains is minor and is <1 wt% for each oxide (Fig. 4). Grain PH13A A2 shows brighter and darker areas in the BSE image but lacks changes in major element compositions (Fig. 4e). The water contents are 1.82 ± 0.15 to 1.72 ± 0.14 wt% (PH13A A1), 1.51 ± 0.12 to 1.55 ± 0.13 wt% (PH13A A2;

457 determined after SMS data collection), 1.47 ± 0.12 (MC18-2), 1.35 ± 0.1 to 1.12 ± 0.09
458 (SH315-4), and 0.65-0.60 ± 0.5 (LF02-042; Figs. 3 and 4). After SMS analysis, grain
459 PH13A A1 was removed from the plexiglass slide and fixed in indium for a second
460 water-content analysis. The water contents in the area of the previous SIMS and the SMS
461 analyses are 1.72 ± 0.12 to 1.91 ± 0.13 wt%, similar to the values measured before SMS
462 analyses. The hydrogen isotope composition of grain MC18-2 is $\delta$D = -91 ± 1‰ (Fig.
463 4a). LF02-042 shows heavier values in the center ($\delta$D = +25 ± 3‰) than at the edge ($\delta$D
464 = +2.7 ± 4‰; Fig. 4b). SH315-4 shows similar values in two areas: -84 ± 1 ‰ and -86 ±
465 2 ‰ (Fig. 4c). PH13A A1 has slightly lighter composition in its center ($\delta$D = -51 ± 2‰)
466 than its edge ($\delta$D = -45 ± 2‰; Fig. 4d).
467
468 **Single-crystal X-ray diffraction**
469 Unit cell dimensions of our amphiboles match the range reported for calcic
470 amphiboles (space group *C*2/*m*; Hawthorne and Oberti 2007; Supplementary Table 1).
471 Cell volumes range from 899 (SH315-4), 907 (PH13A A2), 906 (LF02-042), 911
472 (PH13A A1) to 915 (MC18-2) Å$^3$. Beta angles vary from 104.7° (PH13A A2), 104.8°
473 (MC18-2) to 105.0° (LF02-042), 105.1° (PH13A A1) and 105.5° (SH325-4).
474
475 **Single-crystal synchrotron Mössbauer spectroscopy**
476 We attempted to fit all spectra for each grain, i.e. those collected in different
477 orientations and during different data collection setups, with a similar model. Spectra
478 were fitted first with a texture coefficient of 100%, i.e. with no randomly orientated
479 hyperfine fields, appropriate for single crystals. In a final step, the texture coefficient was

fitted. This yielded improved fits for some spectra. Supplementary Table 1 lists the best-fit hyperfine parameters, thickness, and canting angles. Supplementary Figure 2 shows best-fit results of dual fits with data and reference foil. Uncertainties for the weight fractions of the $Fe^{2+}$ and $Fe^{3+}$ sites of each fit reflect correlations between sites and are given in Supplementary Table 1. The average $Fe^{3+}/Fe^{T}$ ratio for each grain is calculated from spectra collected in the same area and takes into account error propagation. Supplementary Table 5 shows correlation matrices for grains LF02-042 and MC18-2 as an example for a ferric- and ferrous-rich grain.

Spectra of grain MC18-2 were fitted with five sites; these are (site and site weight): $Fe^{2+}$ M(1) with 10-17%, $Fe^{2+}$ M(2) with 45–55%, $Fe^{2+}$ M(3) with 16–30%, $Fe^{3+}$ M(2) with 2–5%, and $Fe^{3+}$ M(3) with 9–13% (Fig. 5). This combination of sites yielded the lowest $\chi^2$ for both the 24-bunch and hybrid mode spectra. Calculated $Fe^{3+}/Fe^{T}$ ratios are $0.13 \pm 0.02$ to $0.14 \pm 0.02$.

Spectra of grain LF02-042 were fitted with four sites: $Fe^{2+}$ M(1) with 8–9%, $Fe^{2+}$ M(3) with 5%, $Fe^{3+}$ M(2) with 46–55%, and $Fe^{3+}$ M(3) with 32–40%. This combination of sites yielded the lowest $\chi^2$ for both the 24-bunch and hybrid mode spectra (Fig. 6) and $Fe^{3+}/Fe^{T}$ ratios of $0.86 \pm 0.09$ to $0.87 \pm 0.12$.

Spectra of grain SH315-4 were fitted with five sites: $Fe^{2+}$ M(1) with 12–18%, $Fe^{2+}$ M(2) with 6–7 %, $Fe^{2+}$ M(3) with 14–20%, $Fe^{3+}$ M(2) with 25–40 %, and $Fe^{3+}$ M(3) with 23–36%. The hybrid time domain spectrum of SH315-4 was fitted with three additional sites: a polycrystalline $Fe^{2+}$ site accounting for twinning at M(2) and M(3), and two sites accounting for disordered magnetic oxides of low weight 1–13%, which occur as inclusions, and observed in the hybrid energy domain spectrum; the $Fe^{3+}/Fe^{T}$ ratios are

503 0.58±0.02 to 0.63±0.03 (Fig. 7). Spots 2 and 3, analyzed in different areas (Fig. 4c),
504 yielded $Fe^{3+}/Fe^{T}$ ratios of 0.51 ± 0.02 to 0.59 ± 0.02, respectively.

505 Spectra of grain PH13A A2 were fitted with five sites: $Fe^{2+}$ M(1) with 7–9%, $Fe^{2+}$
506 M(2) with 52–56 %, $Fe^{2+}$ M(3) with 16–19%, $Fe^{3+}$ M(2) with 13–14 %, and $Fe^{3+}$ M(3)
507 with 7%. Orientations 1 and 2 analyzed during hybrid mode yielded similar fits (Fig. 8).
508 The $Fe^{3+}/Fe^{T}$ ratios are 0.20 ± 0.03 to 0.21 ± 0.01.

509 Spectra of grain PH13A A1 were fitted with four sites: $Fe^{2+}$ M(1) with 3–14%,
510 $Fe^{2+}$ M(3) with 22–34%, $Fe^{3+}$ M(2) with 58–61 %, and $Fe^{3+}$ M(3) with 1–11%. The
511 $Fe^{3+}/Fe^{T}$ ratios range from 0.61 ± 0.01 to 0.64 ± 0.03 (Fig. 9).

512 Supplementary Figure 3 shows additional fitted spectra not displayed in Figures 5
513 to 9. Additionally, we also calculated energy domain spectra from measured energy
514 domain spectra of MC18-2 and SH315-4 (Figs. 5 and 9) and time domain spectra of
515 PH13A A1 (Fig. 9) using the CONUSS software.

516 The IS and QS ranges are in general agreement with those determined by
517 conventional Mössbauer spectroscopy (Fig. 10). IS are larger for $Fe^{2+}$ (~0.9–1.2 mm/s;
518 Fig. 10a-c) than for $Fe^{3+}$ (~0.25–0.45 mm/s; Fig. 10d, e). QS of the $Fe^{2+}$ sites of grains
519 SH315-4, MC18-2, PH13A A1, and PH13A A2 increase in the following order:
520 M(1)>M(3)>M(2) in accordance with literature data (Fig. 10a-c; Supplementary Table 4).
521 Grain LF02-042 shows a QS at the M(3) site that is larger compared to M(1). QS of the
522 $Fe^{3+}$ M(3) site in this grain is larger compared to the M(2) site in agreement with
523 literature data. The difference in QS between M(3) and M(2) is minimal for grain SH315-
524 4 (Fig. 10d,e).

525 The EMPA, SIMS, and SMS data collected in similar areas on each grain (~50–
526 100 μm$^2$; Fig. 4) allow the correlation of major element composition, $Fe^{3+}/Fe^{T}$ ratio, and
527 water content (oxo-component). An increase in the site weight of $Fe^{2+}$ at M(2) (~0.05 to
528 0.55 apfu) accompanies an increase of the QS of $Fe^{2+}$ at M(1) and M(3) from ~2.5 to 2.8
529 mm/s and 2.1 to 2.4 mm/s, respectively (Fig. 11a,b). The QS of $Fe^{3+}$ at M(2) decreases
530 from ~0.95 to 0.7 mm/s with increasing magnesium content (Fig. 11c). An increase of the
531 oxo-component from ~0.2 to 1.3 apfu correlates with a decrease in the QS of the $Fe^{2+}$
532 M(1) site (~2.9 to 2.2 mm/s; Fig. 11d).
533
534 **Identifying SMS spectral signatures of inclusions**
535 Small percentages of a magnetic inclusion, e.g. 2–15% of magnetite are detectable
536 in the SH315-4 time spectra and energy spectra collected during hybrid mode. Visually,
537 these are the small-scale high-frequency oscillations in the time spectrum (Fig. 7h) and
538 the additional intensity around 4 mm/s in the energy spectrum (Fig. 7i). Improvements of
539 the fits were achieved by introducing additional sites with texture coefficients close to
540 zero, where one site has magnetic hyperfine parameters consistent with reports for
541 magnetite at ambient conditions (e.g., Glazyrin et al. 2012), but large FWHM values
542 suggesting significant degrees of non-crystallinity (Supplementary Table 1).
543 Iron oxide inclusions can be <10 μm (Fig. 4 and results section) and spectra
544 collected in different orientations without the Cu aperture may not have been collected on
545 exactly the same spot. This explains why a small percentage of magnetite is necessary to
546 fit the hybrid mode but not the 24-bunch mode spectra of grain SH315-4. Similarly,
547 hyperfine parameters and site weights can vary slightly between spectra collected on the

548 same grain in a similar area but not exactly at the same spot. These variations are
549 minimal (Supplementary Table 1) and can be explained by a spatial deviation of several
550 micrometers.
551
552 **Discussion**
553 **Magmatic versus dehydrogenated amphiboles**
554 The reddish color, low water content (0.60-0.65 wt%), and heavy hydrogen
555 isotope composition ($\delta$D = +2-25 ‰ relative to SMOW) of grain LF02-042 compared to
556 other grains indicate that it underwent post-crystallization dehydrogenation. The loss of
557 $H_2$ from the amphibole structure is associated with the oxidation of iron and a shift to
558 heavier H isotope compositions (Fig. 3b). We modeled Rayleigh fractionation of
559 hydrogen isotopes during dehydrogenation of an amphibole crystal. A water content of
560 1.65 wt% and a δD value of -85‰ was chosen as a starting amphibole composition. This
561 water content is similar to non-dehydrogenated grains analyzed from this sample
562 (unpublished). In addition, this starting δD value is typical for arc magmas determined
563 from melt inclusions (-95 to -12‰; Shaw et al. 2008; Walowski et al. 2015; Fig. 3b). We
564 are able to reproduce the LF02-042 data with a -80‰ to -100‰ fractionation between $H_2$
565 vapor and amphibole (Fig. 3b). Amphibole-$H_2$ vapor fractionation factors are not well
566 constrained experimentally (e.g., Venneman and O'Neil, 1996 and references therein),
567 but the values used in the modeling are of the same sign and magnitude as those
568 established by previous experimental studies (between -25 to -200‰; Kuroda et al.,
569 1988). In any case, the high $Fe^{3+}$ content (32-40%) on the M(3) site of sample LF02-042

570 is interpreted as the result of extensive dehydrogenation and associated oxidation of $Fe^{2+}$
571 previously occupying this site.

572 None of the grains have a fully occupied W-site (Cl, F, OH) but contain an oxo-
573 component ($O^{2-}$ on the W-site): SH315-4, 0.54 ± 0.09 apfu; LF02-042, 1.32 ± 0.05 apfu;
574 MC18-2, 0.23 ± 0.12 apfu; PH13A A1, 0.18 ± 0.13 apfu. We interpret the presence of an
575 oxo-component, i.e. a low volatile content, in SH315-4, MC18-2, and PH13A A1 in
576 combination with arc magmatic hydrogen isotope compositions (Fig. 3b) as reflecting
577 primary crystallization conditions. The oxo-component in these grains can be a result of
578 crystallization under low water activity and/or under very oxidized conditions (i.e., high
579 $Fe^{3+}/Fe^{T}$ in the melt).

580

581 **Comparison with conventional Mössbauer studies**

582 Figure 10 shows a comparison of QS and IS of amphiboles determined by
583 conventional MB spectroscopy with our results. Identification of peaks and assignment to
584 specific crystallographic sites in conventional MB spectra is hindered by peak overlap
585 (e.g., Burns and Greaves 1971). SMS measurements of single crystals permit access to
586 the polarization dependence of the electric field gradient for specific crystallographic
587 sites through the calculation and assignment of Euler angles. Thus, our data provide an
588 opportunity to test previous site assignments.

589 Both methods generally agree on the range of QS and IS (Fig. 10). However, we
590 find no high IS (>1.2 mm/s; Fig. 10a, b, c) for any of the $Fe^{2+}$ sites as suggested by
591 Bancroft and Brown (1975) for hornblende. In general, the QS for the $Fe^{2+}$ sites in
592 conventional MB are assigned based on the assumption of a negative correlation between

593 $Fe^{2+}$ and distortion from the ideal octahedral geometry (Ingalls 1964; Dowty and
594 Lindsley 1973), and the QS are as follows: M(1)>M(3)>M(2) (grey boxes in Fig. 10
595 show the range of QS and IS for specific crystallographic sites as ascribed by
596 conventional MB). The samples we investigated support this trend, with the exception of
597 grain LF02-042, which shows $Fe^{2+}$ QS of M(3)>M(1) (no $Fe^{2+}$ occupancy on the M(2)
598 site; Fig. 10a, c). We show that LF02-042 is strongly dehydrogenated. Unlike M(2), the
599 M(1) and M(3) sites are adjacent to the O(3) sites in the amphibole structure, which
600 contain OH and can form an oxo-component through the oxidation of Fe on these sites
601 (e.g., Phillips et al. 1989). We thus interpret the QS of M(3)>M(1) for grain LF02-042 as
602 a result of oxidation. This likely causes a decrease of the QS at M(1) due to an increased
603 distortion of this site. A full structure refinement is necessary to fully verify this.
604 Oxidation of $Fe^{2+}$ at M(1) and an associated decrease in QS during dehydrogenation in a
605 riebeckite amphibole structure has also been shown by Oberti et al. (2018).

606 The results of the Euler angle calculations show that the angles of the M(1) and
607 M(2) sites are very similar (Supplementary Table 3). Thus, the distinguishing feature of
608 these sites is the difference in QS both for $Fe^{2+}$ and $Fe^{3+}$. This is in agreement with
609 conventional MB studies, which generally assign M(2) a smaller QS (Fig. 10b) compared
610 to the M(1) site (Fig. 10a) based on lattice distortion (e.g., Hawthorne et al 1983).

611 Charge balance calculations allow one to estimate the amount of $Fe^{2+}$ on the M(4)
612 site, if the water content of the amphibole is known. For amphiboles investigated in this
613 study, we are able to calculate the amount of $Fe^{2+}$ on the M(4) using charge balance and
614 the water content determined by SIMS. Ferrous iron varies from 0.02 to 0.11 apfu on the
615 M(4) site. We note that introducing a $Fe^{2+}$ M(4) site in our model does not improve the

616 fitting of our spectra, which is supported by charge balance considerations suggesting
617 $Fe^{2+}$ only occurs in small quantities on the M(4) site (≤0.11 apfu) in our samples.
618 Previous studies using conventional MB (e.g., Goldman 1979; Iezzi et al. 2003; Driscall
619 et al. 2005), however, indicate the presence of $Fe^{2+}$ at the M(4) site. We do not find
620 strong evidence for this in the present study based on our fitting models. A full structural
621 refinement would clarify the magnitude of $Fe^{2+}$ on the M(4) site.

622 Energy-domain spectra collected with our new setup allows a comparison to
623 conventional MB energy-domain spectra. We compare sample MC18-2 to two calcic
624 amphibole conventional MB spectra comprising similar $Fe^{3+}/Fe^{T}$ ratios: 0.25 (sample
625 BCc-13; Bancroft & Brown, 1975; FeO: 17.09 wt%) and 0.17 (sample A2; Schmidbauer
626 et al., 2000; FeO: 21.01 wt%). All spectra (MC18-2 and published spectra) consist of one
627 doublet with broad lines due to the dominance of $Fe^{2+}$. An additional weak component
628 ('shoulder') occurs due to $Fe^{3+}$. Published amphibole spectra are fitted with 4 sites: three
629 $Fe^{2+}$ and one $Fe^{3+}$. While Bancroft & Brown (1975) ascribe $Fe^{2+}$ to different
630 crystallographic sites according to decreasing QS (M(1)>(M3)>M(2)), Schmidbauer et al.
631 (2000) ascribed the smallest ferrous QS (1.91 mm/s) to M(3). Our spectra, on the other
632 hand is fitted with 5 sites (three $Fe^{2+}$ and two $Fe^{3+}$) and ferrous QS decrease similarly
633 from M(1) to M(3) and M(2). While general ranges in QS and IS are similar between our
634 study and published fits, the presence of an additional $Fe^{3+}$ site in our data is justified due
635 to the fact that we consider both the energy and time domain of multiple orientations to
636 arrive at the best model to explain the hyperfine parameters. This approach has never
637 been done before this study. We further calculated energy domain spectra from time
638 domain spectra for 24-bunch mode data of sample PH13A A1 for orientation 1 and 2

(Fig. 9d,e). These allow a direct comparison of orientation effects. However, analysis of the same amphibole grain with SMS and conventional MB is necessary to fully compare fitting results by both methods.

**Variation of hyperfine parameters with composition**

Previous studies, using a combination of conventional MB spectroscopy and XRD, detected correlations between QS and IS of $Fe^{3+}$and $Fe^{2+}$ and the chemical composition of amphibole grains. Redhammer and Roth (2002) observed an increase in QS of $Fe^{2+}$ at M(1) and M(3) with an increase in the average ionic radius of the M(2) site. In our study, the average ionic radius of the M(2) site cannot be determined without a full structure refinement. However, we can use the site weight of $Fe^{2+}$ at M(2) as a rough proxy for the average ionic radius, as it has the largest radius (0.78 Å in octahedral coordination) of all cations potentially occupying this site ($Mg^{2+}$: 0.72 Å; $Fe^{3+}$: 0.65 Å; $Al^{3+}$: 0.53 Å; $Ti^{4+}$: 0.60 Å). We observe an increase in QS at M(1) and M(3) with an increase in $Fe^{2+}$ occupancy at the M(2) site (Fig. 11a,b). Lower site weights of $Fe^{2+}$ at M(2) indicate the substitution with other cations, which would cause a distortion at this site resulting in lower $Fe^{2+}$ QS.

$Mg^{2+}$–$Fe^{2+}$ substitution in amphibole is common and the Mg/(Mg + $Fe^{2+}$) ratio has been used for nomenclature purposes (e.g., Leake et al. 2004). We observe an increase in Mg (2.4 to 3.2 apfu) at the C-site accompanied by a decrease of QS on the $Fe^{3+}$ M(2) site from ~0.9 to 0.6 mm/s (Fig. 11c). On the contrary, Della Ventura et al. (2016) observed an increase in QS of $Fe^{3+}$ at M(2) with increasing Mg in richterite. Given the known positive correlation between $Fe^{3+}$ QS and the electronic distortion at the octahedral site

(e.g. Della Ventura et al. 2016), this trend can be interpreted as a decrease in distortion by the substitution of Mg. QS of the $Fe^{2+}$ sites and IS of all sites do not show a systematic dependence with Mg concentration.

We observe a decrease in QS of $Fe^{2+}$ at M(1) with increasing oxo-component (Fig. 11d). The formation of an oxo-component is accompanied by shortening of the M-O(3) bond lengths and thus causes an increase in the site distortion, which is reflected in lower QS at the $Fe^{2+}$ M(1) site. There appears to be no systematic change in the QS or IS of the other $Fe^{2+}$ sites.

**Ferric iron accommodation**

Three mechanisms have been proposed to accommodate $Fe^{3+}$ in the amphibole structure (Clowe et al. 1988; Popp et al. 1990; Dyar et al. 1993; King et al. 2000; Oberti et al. 2007):

(1) Oxo-component creation: $Fe^{2+}_{C\text{-site}} + OH^{-}_{W\text{-site}} = Fe^{3+}_{C\text{-site}} + O^{2-}_{W\text{-site}} + {}_{H+}$

(2) Substitution on the octahedral site: $Al^{3+}_{C\text{-site}} = Fe^{3+}_{C\text{-site}}$

(3) A-site vacancy creation: $(Na,K)^{+}_{A\text{-site}} + Fe^{2+}_{C\text{-site}} = {}_{A\text{-site}} + Fe^{3+}_{C\text{-site}}$

Figure 12 illustrates these accommodation mechanisms with data from this study and a literature compilation of studies determining amphibole major element compositions, $Fe^{3+}/Fe^{T}$ ratios, and water content (Supplementary Table 6 lists the data, references, and the method by which data was acquired). No single mechanism can univocally explain $Fe^{3+}$ accommodation in our samples and the literature data. Mechanism 1 appears to be an important process to accommodate $Fe^{3+}$ in LF02-042 and PH13A A2 (and potentially MC18-2 given its proximity to the 1:1 line). However, incorporation of $Ti^{4+}$ can also

685 locally balance the oxo-component (e.g., Oberti et al. 2007; Fig. 12b). The literature data
686 shows that both mechanisms are likely important in mantle-derived amphiboles (see also
687 King et al., 1999; Oberti et al., 2007). In grains LF02-042, MC18-2, and PH13A A2 the
688 oxo-component (1.32 ± 0.05 apfu, 0.23 ± 0.12 apfu, and 0.32 ± 0.12 apfu) can account
689 for all of the $Fe^{3+}$ (1.29 apfu, 0.35 apfu and 0.32 apfu; calculated from EMPA and SMS
690 data) within uncertainty. The difference in the hydrogen isotope compositions of LF02-
691 042 and MC18-2 indicates that the oxo-component in grain MC18-2 is not a consequence
692 of dehydrogenation but might be a result of crystallization under reduced conditions
693 and/or from a melt with low water activity. For grains SH315-4 and PH13A A1, all three
694 mechanisms are required to accommodate the $Fe^{3+}$ content (1.22 and 0.74 apfu). The oxo-
695 component (0.54 ± 0.09 and 0.18 ± 0.13 apfu) alone cannot accommodate the amount of
696 $Fe^{3+}$ (even if iron oxidation is the sole charge balance mechanism). In addition to the oxo-
697 component, a combination of A-site vacancies and substitution of $Fe^{3+}$ for $Al^{3+}$ on the C-
698 site is required (Fig. 12c,d). As both grains do not show signs of post-crystallization
699 dehydrogenation, we conclude that the combination of all accommodation mechanisms
700 occurred during crystallization and were controlled by crystallization pressure (Al
701 incorporation into the amphibole), water activity in the melt (oxo-component), and melt
702 composition (Na and K content).

703 The literature data shown in Fig. 12 do not reveal a clear dominance of one $Fe^{3+}$
704 accommodation mechanism. We speculate here, that this may be due to (a) bulk
705 techniques averaging intra-grain compositional heterogeneities and inclusions (e.g.,
706 biotite); (b) different amphibole groups favor different accommodation mechanism
707 depending on their composition (e.g., mantle-derived amphiboles, Figure 12a, b); (c) that

several accommodation mechanism are required to account for all $Fe^{3+}$; and (d) individual grains have been variably effected by dehydrogenation. Therefore, experimental amphiboles synthesized under controlled conditions are the best candidates to understand ferric iron accommodation mechanisms.

**Intra-grain heterogeneities in $Fe^{3+}/Fe^{T}$ ratios**

Igneous amphiboles commonly show intra-grain zonation in major and trace elements, often used to infer magmatic processes (e.g., Barnes et al. 2016; Kiss et al. 2014). Thus, it is reasonable to assume that $Fe^{3+}/Fe^{T}$ ratios vary within single grains, recording changes in crystallization conditions and/or post-crystallization oxidation. The high-spatial resolution of SMS allows detecting these variations.

Two areas on grain SH315-4 were analyzed: the center of the grain (Fig. 4c) yielded $Fe^{3+}/Fe^{T}$ ratios of 0.59 ± 0.02 to 0.63 ± 0.02 generally higher than two spots close to the edge (spots 2 and 3; 0.51± 0.02 and 0.59 ± 0.02, respectively; Fig. 4c). Attempts to fit spectra from both areas with the same model failed; instead, lower $Fe^{3+}/Fe^{T}$ ratios for spot 2 and 3 compared to the area in the center were required indicating intra-grain heterogeneity in $Fe^{3+}/Fe^{T}$ ratios. In combination with the major element data, this could be related to magmatic or post-eruption processes. For example, dacites from the June 1991 eruption of Mt. Pinatubo contain amphibole phenocrysts with cores rich in $Al_2O_3$ and $TiO_2$ (e.g., Bernard et al. 1996; Scaillet et al. 1999; Fig. 4d), either due to an early mixing event or a higher-pressure crystallization stage prior to eruption (Prouteau & Scaillet, 2003; Scaillet et al. 1999). Grain PH13A A1 represents an example of a high-$Al_2O_3$ core, whereas grain PH13A A2 exemplifies a rim or low-$Al_2O_3$ phenocryst.

Although not analyzed in the same grain, SMS is able to capture a difference in $Fe^{3+}/Fe^{T}$ ratios between high-$Al_2O_3$ cores with 0.62 ± 0.01 (PH13A A1) and low-$Al_2O_3$ rims/phenocrysts with 0.20 ± 0.01 (PH13A A2).

A comparison of our data with those of Underwood et al. (2012; 2013) shows the importance of a high-spatial resolution technique such as SMS to distinguish intra-grain compositional heterogeneities and to avoid the analysis of inclusions. Underwood et al. analyzed amphibole grains from samples LF02-042 and SH315-4, using wet chemistry on aliquots of multiple grains. Their analyses yielded for LF02-042: $Fe^{3+}/Fe^{T}$: 0.56, $H_2O$: 2.3 wt%, δD: -68 ‰, and for SH315-4: $Fe^{3+}/Fe^{T}$: 0.99, $H_2O$: 1.7 wt%, δD: -86 ‰ significantly different from the values obtained in our study. It is likely that the samples contain mixed crystal populations (e.g., with grains with different degrees of dehydrogenation) such that the results from our and their studies cannot be directly related. However, the elevated water contents of 2.3 wt% measured by Underwood et al. (2012) in LF02-042 may suggest the analysis of amphibole with biotite inclusions, which are abundant in this sample.

A mixed analysis of amphibole and biotite, multiple crystal populations (as in the case of PH13A A1) as well as iron oxides would yield higher $Fe^{3+}/Fe^{T}$ ratios than the amphibole alone. We demonstrated this with SMS energy- and time-domain spectra collected for SH315-4 that exhibited signatures from an inclusion characterized by magnetic ordering (see results section).

**Comparison with other methods determining $Fe^{3+}/Fe^{T}$ ratios in amphibole**

753 Other methods have been used to determine the $Fe^{3+}/Fe^{T}$ ratios in amphibole with
754 a similar high-spatial resolution. The most common applied are XANES (X-ray
755 absorption near edge structure spectroscopy; e.g., Dyar et al. 2016) and EMPA (e.g., Li et
756 al. 2019), which use spot sizes of $7 \times 9$ μm (Dyar et al. 2016; but spots sizes of ~2-5 $\mu m^2$
757 are possible and applied to glass analyses; McCanta et al. 2017) and $20 \times 20$ μm (e.g., Li
758 et al. 2019), respectively. While X-ray photoelectron spectroscopy (XPS) (e.g., Fantauzzi
759 et al. 2010) and electron energy-loss spectroscopy (EELS) have been used to analyze
760 surface $Fe^{3+}/Fe^{T}$ ratios, the latter has been shown to probe on the nanometer scale (e.g.,
761 Garvie and Busek 1998). Other methods such as the Mössbauer milliprobe allow the
762 analyses of small sample sizes (as small as ~50 μm; McCammon 1994), however this
763 method has not been applied to amphiboles. XANES, EMPA, EELS, and XPS require the
764 use of reference material for data interpretation. Dyar et al (2002), for example, used
765 fayalite, magnetite, hematite, and aegirine with known $Fe^{3+}/Fe^{T}$ ratios, determined by
766 conventional MB spectroscopy and/or wet chemistry to study amphiboles using XANES.
767 No well-characterized reference material exists for calcic amphibole. SMS and other
768 Mössbauer setups (e.g., Mössbauer millioprobe) do not require reference spectra,
769 therefore eliminating dependency on accuracy of reference material values. Other
770 advantages of SMS over conventional MB spectroscopy are a linear polarization of the
771 source and shorter data collection time on natural amphiboles (samples not enriched with
772 $^{57}Fe$). The conventional MB source emits unpolarized radiation, which significantly
773 reduces the spectral sensitivity to electric-field-gradient tensor orientation in single
774 crystals. While conventional MB spectroscopy requires multiple-day data collection, the
775 spectra in this study were obtained in 1 to 12 hours. Finally, the ability to measure both

776 energy spectra (with a polarized source) and time spectra (with an extended time
777 window) at the same microns-sized spot offers a notable advantage over conventional
778 MB spectroscopy, especially when measuring samples containing multi-valent iron and
779 with multiple sites, as was done here.

780 Beam-induced iron oxidation was documented in hydrous glass using XANES
781 (synchrotron radiation; Cottrell et al. 2018) and in amphibole using EMPA (electron
782 beam; Li et al., 2019). Beam-induced damage is not only a function of beam power
783 density (flux density) but also of sample thickness and composition (e.g., water content),
784 and the accumulated dose (i.e., flux times exposure time). During our SMS analyses, the
785 flux density was $1.7 \times 10^7$ and $1.0 \times 10^{10}$ photons/s/μm$^2$ during the 24-bunch mode and
786 the hybrid time mode, respectively. The flux during the collection of the energy domain
787 spectra was negligible because the incident bandwidth on the sample was very small ($10^{-8}$
788 eV). Cottrell et al. (2018) argued that at flux of $\leq 6 \times 10^7$ photons/s/μm$^2$ the oxidation
789 effect is negligible. This flux is higher than the one used during our 24-bunch mode
790 experiments; however, the results by Cottrell et al (2018) cannot be directly compared to
791 our data as the composition, structure, thickness, and water content of our samples are
792 different. XANES studies of amphiboles by Bajit et al. (1994), Delaney et al. (1996), and
793 Dyar et al. (2002, 2016) do not provide information regarding beam flux during data
794 collection, nor did they consider beam-induced iron oxidation. However, the agreement
795 between XANES and conventional MB and/or wet chemistry results in these past studies
796 suggests that beam-induced oxidation is minimal. The fact that we have been able to fit
797 the hybrid mode and 24-bunch mode spectra with very similar models support the notion
798 that beam-induced oxidation can be neglected in the current study. We also analyzed

grain PH13A A1 twice for water content at the same area: before and after SMS data collection. The data shows no difference before (1.72 ± 0.14 wt%) and after (1.79 ± 0.13 wt%; average of three analyses) SMS data collection. However, a more detailed and systematic study assessing beam-damage study should be undertaken.

## Implications

The workflow presented in this study combining multiple high-spatial resolution techniques (EMPA, SIMS, and SMS) on the same area of individual amphibole grains allows distinguishing between post-crystallization and crystallization effects of Fe oxidation. This is crucial if analyzed $Fe^{3+}/Fe^{T}$ ratios are to be used to infer the conditions during amphibole formation. Natural igneous amphiboles erupted in arc volcanoes for example can show intra-grain compositional zonation (e.g., Gorbach et al. 2020), which can reflect distinct crystallization conditions and levels in a vertically extensive magma plumbing system (e.g., Humphreys et al., 2019). Resolving these conditions is crucial for an understanding of the evolution of magmatic systems. In particular, variations in the $Fe^{3+}/Fe^{T}$ ratios in a melt can be recorded by the $Fe^{3+}/Fe^{T}$ ratios in amphiboles during crystallization (e.g., King et al. 2001). The high spatial-resolution and relatively low uncertainties of the SMS analysis allow for the detection of small variations in $Fe^{3+}/Fe^{T}$ ratios within individual grains and in combination with results from EMPA and SIMS, these can be attributed to changing crystallization conditions or the effects of post-crystallization oxidation. Future work should use electron backscatter diffraction to determine the lattice orientation of amphiboles in thick sections; this will allow SMS analysis in a textural context.

822 Furthermore, SMS distinguishes between specific crystallographic sites in the
823 amphibole structure occupied by $Fe^{2+}$ and $Fe^{3+}$. In combination with other methods, such
824 as infrared spectroscopy and XRD, SMS is a promising avenue to improve our
825 understanding of the structural changes in amphibole accompanying dehydrogenation and
826 the general long-range order of iron as a function of mineral chemistry.
827

828 **Acknowledgments**

829 The authors thank Yunbin Guo (Caltech), Larry Henling (Caltech), and Chi Ma (Caltech)
830 for assistance with SIMS, XRD, and EMPA analyses, respectively. Johannes Buchen,
831 Vasilije Dobrosavljevic, Olivia Pardo, Mary Peterson, and Emma Sosa (all Caltech)
832 helped during in-person and remote beamtime at Argonne National Laboratory. Sandy
833 Underwood (Montana State University), Carl Thornber (USGS), and Kevin Schrecengost
834 (UC Davis) shared sample material, which made this study possible. We also thank
835 Darby Dyar, David Jenkins, and an anonymous reviewer for their helpful and
836 constructive reviews, which improved this manuscript. This work was supported by NSF
837 grant 1841790 to C. E. Bucholz and J. M. Jackson. This research used resources of the
838 Advanced Photon Source, a U.S. Department of Energy (DOE) Office of Science User
839 Facility operated for the DOE Office of Science by Argonne National Laboratory under
840 Contract No. DE-AC02-06CH11357.
841

842 **References**

Abdu, Y. A., and Hawthorne, F. C. (2009) Crystal Structure and Mössbauer spectrsocopy of tschermakite from the ruby locality at Fiskenaesset, Greenland. The Canadian Mineralogist, 47, 917-926.

Armstrong, J. T. (1995) CITZAF-a package of correction programs for the quantitative Electron Microbeam X-Ray-Analysis of thick polished materials, thin-films, and particles. Microbeam Analysis, 4, 177-200.

Bajt, S., Sutton, S., and Delaney, J. (1994) X-ray microprobe analysis of iron oxidation states in silicates and oxides using X-ray absorption near edge structure (XANES). Geochimica et Cosmochimica Acta, 58, 5209-5214.

Bancroft, G. M., and Brown, J. R. (1975) A Mössbauer study of coexisting hornblendes and biotites: quantitative $Fe^{3+}/Fe^{2+}$ ratios. American Mineralogist, 60, 265-272.

Bancroft, G. M., and Burns, G. R. (1969) Mössbauer and absorption spectral study of alkali amphiboles. Mineralogical Society of America Special Paper, 2, 137-148.

Barnes, C. G., Memeti, V., and Coint, N. (2016) Deciphering magmatic processes in calc-alkaline plutons using trace element zoning in hornblende. American Mineralogist, 101, 328-342.

Bernard, A., Knittel, U., Weber, B., Weis, D., Albrecht, A., Hattori, K., Klein, J., and Oles, D. (1996) Petrology and geochemistry of the 1991 eruption products of Mount Pinatubo. Fire and mud: eruptions and lahars of Mount Pinatubo, Philippines, 767-797.

Boyce, J. W., Liu, Y., Rossman, G. R., Guan, Y., Eiler, J. M., Stolper, E. M., and Taylor, L. A. (2010) Lunar apatite with terrestrial volatile abundances. Nature, 466, 466-469.

866 Bruker (2012a) APEX3. Bruker AXS inc., Madison, WI, USA.

867 Bruker (2012b) CELL_NOW. Bruker AXS inc., Madison, WI, USA.

868 Burns, R. G., and Greaves, C. (1971) Correlations of infrared and Mössbauer site
869 population measurements of actinolites. American Mineralogist, 56, 2010-2033.

870 Chin, E. J., Soustelle, V., Hirth, G., Saal, A. E., Kruckenberg, S. C., and Eiler, J. M.
871 (2016) Microstructural and geochemical constraints on the evolution of deep arc
872 lithosphere. Geochemistry, Geophysics, Geosystems, 17, 2497-2521.

873 Clowe, C. A., Popp, R. K., and Fritz, S. J. (1988) Experimental investigation of the effect
874 of oxygen fugacity on ferric-ferrous ratios and unit-cell parameters of four natural
875 clinoamphiboles. American Mineralogist, 73, 487-499.

876 Clynne, M. A., and Muffler, L. J. P., (2010) Geologic map of Lassen Volcanic National
877 Park and vicinity, California, US Department of the Interior, US Geological
878 Survey.

879 Cottrell, E., Lanzirotti, A., Mysen, B., Birner, S., Kelley, K. A., Botcharnikov, R., Davis,
880 F. A., and Newville, M. (2018) A Mössbauer-based XANES calibration for
881 hydrous basalt glasses reveals radiation-induced oxidation of Fe. American
882 Mineralogist,103, 489-501.

883 Crowley, J., Schoene, B., and Bowring, S. (2007) U-Pb dating of zircon in the Bishop
884 Tuff at the millennial scale. Geology, 35, 1123-1126.

885 Delaney, J. S., Dyar, M. D., Sutton, S. R., and Bajt, S. (1998) Redox ratios with relevant
886 resolution: Solving an old problem by using the synchrotron micro-XANES
887 probe. Geology, 26, 139-142.

888 Della Ventura, G., Mihailova, B., Susta, U., Cestelli Guidi, M., Marcelli, A., Schlüter, J.,
889 and Oberti, R. (2018) The dynamics of Fe oxidation in riebeckite: A model for
890 amphiboles. American Mineralogist, 103, 1103-1111.
891 Della Ventura, G., Redhammer, G. J., Iezzi, G., Hawthorne, F. C., Papin, A., and Robert,
892 J.-L. (2005) A Mössbauer and FTIR study of synthetic amphiboles along the
893 magnesioriebeckite–ferri-clinoholmquistite join. Physics and Chemistry of
894 Minerals, 32, 103-113.
895 Della Ventura, G., Redhammer, G. J., Robert, J.-L., Sergent, J., Iezzi, G., and Cavallo, A.
896 (2016) Crystal-Chemistry of Synthetic Amphiboles Along the Richterite–Ferro-
897 Richterite Join: A Combined Spectroscopic (FTIR, Mössbauer), XRD, and
898 Microchemical Study. The Canadian Mineralogist, 54, 97-114.
899 Deloule, E., France-Lanord, C., and Albarede, F. (1991) D/H analysis of minerals by ion
900 probe. Stable Isotope Geochemistry: A Tribute to Samuel Epstein, 3, 53-62.
901 Dauphas, N., Roskosz, M., Alp, E. E., Golden, D. C., Sio, C. K., Tissot, F. L. H., Hu, M.
902 Y., Zhao, J., Gao, L., Morris, R. V. (2012). A general moment NRIXS approach
903 to the determination of equilibrium Fe isotopic fractionation factors: application
904 to goethite and jarosite. Geochimica et Cosmochimica Acta, 94, 254-275.
905 Dowty, E., and Lindsley, D. (1973) Mössbauer spectra of synthetic hedenbergite-
906 ferrosilite pyroxenes. American Mineralogist, 58, 850-868.
907 Driscall, J., Jenkins, D. M., Dyar, M. D., and Bozhilov, K. N. (2005) Cation ordering in
908 synthetic low-calcium actinolite. American Mineralogist, 90, 900-911.

909 Dyar, M. D., Agresti, D. G., Schaefer, M. W., Grant, C. A., and Sklute, E. C. (2006)
910 Mössbauer spectroscopy of earth and planetary materials. Annual Review of
911 Earth and Planetary Sciences, 83-125.
912 Dyar, M. D., Breves, E. A., Gunter, M. E., Lanzirotti, A., Tucker, J. M., Carey, C., Peel,
913 S. E., Brown, E. B., Oberti, R., and Lerotic, M. (2016) Use of multivariate
914 analysis for synchrotron micro-XANES analysis of iron valence state in
915 amphiboles. American Mineralogist, 101, 1171-1189.
916 Dyar, M. D., Lowe, E. W., Guidotti, C. V., and Delaney, J. S. (2002) $Fe^{3+}$ and $Fe^{2+}$
917 partitioning among silicates in metapelites: A synchrotron micro-XANES study.
918 American Mineralogist, 87, 514-522.
919 Dyar, M. D., Mackwell, S. J., McGuire, A. V., Cross, L. R., and Robertson, J. D. (1993)
920 Crystal chemistry of $Fe^{3+}$ and $H^{+}$ in mantle kaersutite: Implications for mantle
921 metasomatism. American Mineralogist, 78, 968-979.
922 Ernst, W., and Wai, C. (1970) Mössbauer, infrared, X-ray and optical study of cation
923 ordering and dehydrogenation in natural and heat-treated sodic amphiboles.
924 American Mineralogist, 55, 1226-1258.
925 Fantauzzi, M., Pacella, A., Atzei, D., Gianfagna, A., Andreozzi, G. B., & Rossi, A.
926 (2010) Combined use of X-ray photoelectron and Mössbauer spectroscopic
927 techniques in the analytical characterization of iron oxidation state in amphibole
928 asbestos. Analytical and Bioanalytical Chemistry, 396, 2889-2898.
929 Fultz, B. (2002) Mössbauer spectrometry. Characterization of materials, 1-21.
930 Glazyrin, K., McCammon, C., Dubrovinsky, L., Merlini, M., Schollenbruch, K.,
931 Woodland, A., and Hanfland M. (2012) Effect of high pressure on the crystal

932 structure and electronic properties of magnetite below 25 GPa. American
933 Mineralogist, 97, 128–133.
934 Goldman, D. S., and Rossman, G. R. (1977) The identification of $Fe^{2+}$ in the M (4) site of
935 calcic amphiboles. American Mineralogist, 62, 205-216.
936 Goldman, D. S. (1979) A reevaluation of the Mössbauer spectroscopy of calcic
937 amphiboles. American Mineralogist, 64, 109-118.
938 Gorbach, N., Philosofova, T., and Portnyagin, M. (2020) Amphibole record of the 1964
939 plinian and following dome-forming eruptions of Shiveluch volcano, Kamchatka.
940 Journal of Volcanology and Geothermal Research, 407, 107108.
941 Hawthorne, F. (1983) Quantitative characterization of site-occupancies in minerals.
942 American Mineralogist, 68, 287-306.
943 Hawthorne, F. C., and Oberti, R. (2007) Amphiboles: crystal chemistry. Reviews in
944 Mineralogy and Geochemistry, 67, 1, 1-54.
945 Hawthorne, F. C., Oberti, R., Harlow, G. E., Maresch, W. V., Martin, R. F., Schumacher,
946 J. C., and Welch, M. D. (2012) Nomenclature of the amphibole supergroup.
947 American Mineralogist, 97, 2031-2048.
948 Hildreth, W. (2004) Volcanological perspectives on Long Valley, Mammoth Mountain,
949 and Mono Craters: several contiguous but discrete systems. Journal of
950 Volcanology and Geothermal Research, 136, 169-198.
951 Hildreth, W., and Mahood, G. A. (1986) Ring-fracture eruption of the Bishop Tuff.
952 Geological Society of America Bulletin, 97, 396-403.
953 Humphreys, M. C., Cooper, G. F., Zhang, J., Loewen, M., Kent, A. J., Macpherson, C.
954 G., and Davidson, J. P. (2019) Unravelling the complexity of magma plumbing at

Mount St. Helens: a new trace element partitioning scheme for amphibole. Contributions to Mineralogy and Petrology, 174, 1, 9.

Iezzi, G., Della Ventura, G., Pedrazzi, G., Robert, J. L., & Oberti, R. (2003) Synthesis and characterisation of ferri-clinoferroholmquistite, $\square Li_2(Fe^{2+}{}_3Fe^{3+}{}_2)Si_8O_{22}(OH)_2$. European Journal of Mineralogy, 15, 321-327.

Ingalls, R. (1964) Electric-field gradient tensor in ferrous compounds. Physical Review, 133, 3A, 787.

Jackson, J. M., Hamecher, E. A., & Sturhahn, W. (2009). Nuclear resonant X-ray spectroscopy of (Mg, Fe) SiO3 orthoenstatites. European Journal of Mineralogy, 21, 551-560.

Johnson, M. C., and Rutherford, M. J. (1989) Experimental calibration of the aluminum-in-hornblende geobarometer with application to Long Valley caldera (California) volcanic rocks. Geology, 17, 837-841.

King, P., Hervig, R., Holloway, J., Delaney, J., and Dyar, M. (2000) Partitioning of $Fe^{3+}/Fe^{total}$ between amphibole and basanitic melt as a function of oxygen fugacity. Earth and Planetary Science Letters, 178, 97-112.

King, P. L., Hervig, R. L., Holloway, J. R., Vennemann, T. W., and Righter, K. (1999) Oxy-substitution and dehydrogenation in mantle-derived amphibole megacrysts. Geochimica et Cosmochimica Acta, 63, 3635-3651.

Kiss, B., Harangi, S., Ntaflos, T., Mason, P. R., and Pál-Molnár, E. (2014) Amphibole perspective to unravel pre-eruptive processes and conditions in volcanic plumbing systems beneath intermediate arc volcanoes: a case study from Ciomadul volcano (SE Carpathians). Contributions to Mineralogy and Petrology, 167, 3, 986.

978 Krawczynski, M. J., Grove, T. L., and Behrens, H. (2012) Amphibole stability in
979 primitive arc magmas: effects of temperature, $H_2O$ content, and oxygen fugacity.
980 Contributions to Mineralogy and Petrology, 164, 317-339.
981 Leake, B. E., Woolley, A. R., Birch, W. D., Burke, E. A., Ferraris, G., Grice, J. D.,
982 Hawthorne, F. C., Kisch, H. J., Krivovichev, V. G., and Schumacher, J. C. (2004)
983 Nomenclature of amphiboles: additions and revisions to the International
984 Mineralogical Association's amphibole nomenclature. Mineralogical Magazine,
985 68, 209-215.
986 Li, X., Zhang, C., Almeev, R. R., Zhang, X.-C., Zhao, X.-F., Wang, L.-X., Koepke, J.,
987 and Holtz, F. (2019) Electron probe microanalysis of $Fe^{2+}/\Sigma Fe$ ratios in calcic and
988 sodic-calcic amphibole and biotite using the flank method. Chemical Geology,
989 509, 152-162.
990 Locock, A. J. (2014) An Excel spreadsheet to classify chemical analyses of amphiboles
991 following the IMA 2012 recommendations. Computers & Geosciences, 62, 1-11.
992 Makino, K., and Tomita, K. (1989) Cation distribution in the octahedral sites of
993 hornblendes. American Mineralogist, 74, 1097-1105.
994 Margulies, S., and Ehrman, J. R. (1961) Transmission and line broadening of resonance
995 radiation incident on a resonant absorber. Nuclear Instrument Methods, 12, 131–
996 37.
997 Margulies, S., DeBrunner, P., and Frauenfelder, H. (1963) Transmission and line
998 broadening in the Mössbauer effect. II. Nuclear Instrument Methods, 21, 217–31.
999 McCammon, C. A. (1994) A Mössbauer milliprobe: Practical considerations. Hyperfine
1000 Interactions, 92, 1235-1239.

1001 McCammon, C., Hutchison, M., and Harris, J. (1997) Ferric iron content of mineral
1002 inclusions in diamonds from Sao Luiz: A view into the lower mantle. Science,
1003 278, 434-436.
1004 McCanta, M. C., Dyar, M. D., Rutherford, M. J., Lanzirotti, A., Sutton, S. R., &
1005 Thomson, B. J. (2017) In situ measurement of ferric iron in lunar glass beads
1006 using Fe-XAS. Icarus, *285*, 95-102.
1007 Miyagi, I., Matsubaya, O., and Nakashima, S. (1998) Change in D/H ratio, water content
1008 and color during dehydration of hornblende. Geochemical Journal, 32, 33-48.
1009 Morrison, R. A., Jackson, J. M., Sturhahn, W., Zhao, J., & Toellner, T. S. (2019). High-
1010 pressure thermoelasticity and sound velocities of Fe-Ni-Si alloys. Physics of the
1011 Earth and Planetary Interiors, 294, 106268.
1012 Mosenfelder, J. L., Le Voyer, M., Rossman, G. R., Guan, Y., Bell, D. R., Asimow, P. D.,
1013 and Eiler, J. M. (2011) Analysis of hydrogen in olivine by SIMS: Evaluation of
1014 standards and protocol. American Mineralogist, 96, 1725-1741.
1015 Mutch, E. J. F., Blundy, J. D., Tattitch, B. C., Cooper, F. J., & Brooker, R. A. (2016) An
1016 experimental study of amphibole stability in low-pressure granitic magmas and a
1017 revised Al-in-hornblende geobarometer. Contributions to Mineralogy and
1018 Petrology, 171,10, 1-27.
1019 Murphy, C. A., Jackson, J. M., & Sturhahn, W. (2013). Experimental constraints on the
1020 thermodynamics and sound velocities of hcp-Fe to core pressures. Journal of
1021 Geophysical Research: Solid Earth, 118, 1999-2016.
1022 Nasir, S., and Al-Rawas, A. D. (2006) Mössbauer characterization of upper mantle
1023 ferrikaersutite. American Mineralogist, 91, 1163-1169.

1024 Ni, P., Zhang, Y., and Guan, Y. (2017) Volatile loss during homogenization of lunar melt
1025 inclusions. Earth and Planetary Science Letters, 478, 214-224.
1026 Oberti, R., Boiocchi, M., Zema, M., Hawthorne, F. C., Redhammer, G. J., Susta, U., and
1027 Della Ventura, G. (2018) The high-temperature behaviour of riebeckite:
1028 expansivity, deprotonation, selective Fe oxidation and a novel cation disordering
1029 scheme for amphiboles. European Journal of Mineralogy, 30, 3, 437-449.
1030 Oberti, R., Hawthorne, F. C., Cannillo, E., and Cámara, F. (2007) Long-range order in
1031 amphiboles. Reviews in Mineralogy and Geochemistry, 67, 125-171.
1032 Ohira, I., Jackson, J. M., Sturhahn, W., Finkelstein, G. J., Kawazoe, T., Toellner, T. S.,
1033 Suzuki, A., Ohtani, E. (2021). The influence of δ-(Al, Fe) OOH on seismic
1034 heterogeneities in Earth's lower mantle. Scientific reports, 11, 1-9.
1035 Pallister, J. S., Hoblitt, R. P., Meeker, G. P., Knight, R. J., and Siems, D. F. (1996)
1036 Magma mixing at Mount Pinatubo: petrographic and chemical evidence from the
1037 1991 deposits. Fire and mud: eruptions and lahars of Mount Pinatubo, Philippines,
1038 687-731.
1039 Pallister, J. S., Thornber, C. R., Cashman, K. V., Clynne, M. A., Lowers, H., Mandeville,
1040 C. W., Brownfield, I. K., and Meeker, G. P. (2008) Petrology of the 2004-2006
1041 Mount St. Helens lava dome--implications for magmatic plumbing and eruption
1042 triggering: US Geological Survey, 2330-7102.
1043 Peters, S. T., Troll, V. R., Weis, F. A., Dallai, L., Chadwick, J. P., and Schulz, B. (2017)
1044 Amphibole megacrysts as a probe into the deep plumbing system of Merapi
1045 volcano, Central Java, Indonesia. Contributions to Mineralogy and Petrology,
1046 172, 4, 1-20.

1047 Phillips, M. W., Draheim, J. E., Popp, R. K., Clowe, C. A., and Pinkerton, A. A. (1989)
1048 Effects of oxidation-dehydrogenation in tschermakitic hornblende. American
1049 Mineralogist, 74, 764-773.
1050 Popp, R. K., Phillips, M. W., and Harrell, J. A. (1990) Accommodation of $Fe^{3+}$ in natural,
1051 $Fe^{3+}$-rich, calcic and subcalcic amphiboles; evidence from published chemical
1052 analyses. American Mineralogist, 75, 163-169.
1053 Prouteau, G., & Scaillet, B. (2003). Experimental constraints on the origin of the 1991
1054 Pinatubo dacite. Journal of Petrology, 44, 2203-2241.
1055 Redhammer, G., and Roth, G. (2002) Crystal structure and Mössbauer spectroscopy of
1056 the synthetic amphibole potassic-ferri-ferrorichterite at 298 K and low
1057 temperatures (80–110 K). European Journal of Mineralogy, 14, 105-114.
1058 Scaillet, B., and Evans, B. W. (1999) The 15 June 1991 eruption of Mount Pinatubo. I.
1059 Phase equilibria and pre-eruption P–T–$f_{O2}$–f $H_2O$ conditions of the dacite magma.
1060 Journal of Petrology, 40, 381-411.
1061 Schmidbauer, E., Kunzmann, T., Fehr, T., and Hochleitner, R. (2000) Electrical
1062 resistivity and $^{57}Fe$ Mössbauer spectra of Fe-bearing calcic amphiboles. Physics
1063 and Chemistry of Minerals, 27, 347-356.
1064 Schuessler, J. A., Botcharnikov, R. E., Behrens, H., Misiti, V., and Freda, C. (2008)
1065 Oxidation state of iron in hydrous phono-tephritic melts. American Mineralogist,
1066 93, 1493-1504.
1067 Semet, M. P. (1973) A Grystal-Ghemical Study of Synthetic Magnesiohastingsite.
1068 American Mineralogist, 58, 480-494.

1069 Shaw, A., Hauri, E., Fischer, T., Hilton, D., and Kelley, K. (2008) Hydrogen isotopes in
1070 Mariana arc melt inclusions: Implications for subduction dehydration and the
1071 deep-Earth water cycle. Earth and Planetary Science Letters, 275, 138-145.
1072 Solomatova, N. V., Alieva, A., Finkelstein, G. J., Sturhahn, W., Baker, M. B., Beavers,
1073 C. M., Zhao, J., Toellner, T. S., and Jackson, J. M. (2019) High-pressure single-
1074 crystal X-ray diffraction and synchrotron Mössbauer study of monoclinic
1075 ferrosilite. Comptes Rendus Geoscience, 351, 2-3, 129-140.
1076 Solomatova, N. V., Jackson, J. M., Sturhahn, W., Rossman, G. R., and Roskosz, M.
1077 (2017) Electronic environments of ferrous iron in rhyolitic and basaltic glasses at
1078 high pressure. Journal of Geophysical Research: Solid Earth, 122, 8, 6306-6322.
1079 Sturhahn, W. (2000) CONUSS and PHOENIX: Evaluation of nuclear resonant scattering
1080 data. Hyperfine Interactions, 125, 1-4, 149-172.
1081 Sturhahn, W., and Gerdau, E. (1994) Evaluation of Time-Differential Measurements of
1082 Nuclear-Resonance Scattering of X-Rays. Phys. Rev. B, 49, 9285-9294.
1083 Sturhahn, W. (2004) Nuclear resonant spectroscopy. Journal of Physics: Condensed
1084 Matter, 16, 5, S497.
1085 Sturhahn, W. (2005) Nuclear resonant scattering. In F. Bassani, G.L. Liedl, P. Wyder
1086 Eds. Encyclopedia of Condensed Matter Physics, p. 227-234. Elsevier.
1087 Sturhahn, W. (2021) CONUSS (COherent NUclear resonant Scattering by Single
1088 crystals). Open source software, http://www.nrixs.com.
1089 Sturhahn, W., and Jackson, J. M. (2007) Geophysical applications of nuclear resonant
1090 spectroscopy. Geological Society of America – Special papeers, 421, 157.

1091 Taylor, L. A., Logvinova, A. M., Howarth, G. H., Liu, Y., Peslier, A. H., Rossman, G. R.,
1092 Guan, Y., Chen, Y., and Sobolev, N. V. (2016) Low water contents in diamond
1093 mineral inclusions: Proto-genetic origin in a dry cratonic lithosphere. Earth and
1094 Planetary Science Letters, 433, 125-132.
1095 Thornber, C. R., Pallister, J. S., Lowers, H. A., Rowe, M. C., Mandeville, C. W., and
1096 Meeker, G. P. (2008) Chemistry, mineralogy, and petrology of amphibole in
1097 Mount St. Helens 2004–2006 dacite. A volcano rekindled, 2004-2006.
1098 Toellner, T.S. (2000) Monochromatization of synchrotron radiation for nuclear resonant
1099 scattering experiments. Hyperfine Interactions, 125, 3–28.
1100 Toellner, T., Alp, E., Graber, T., Henning, R., Shastri, S., Shenoy, G., and Sturhahn, W.
1101 (2011) Synchrotron Mössbauer spectroscopy using high-speed shutters. Journal of
1102 synchrotron radiation, 18, 2, 183-188.
1103 Treiman, A. H., Boyce, J. W., Greenwood, J. P., Eiler, J. M., Gross, J., Guan, Y., Ma, C.,
1104 and Stolper, E. M. (2016) D-poor hydrogen in lunar mare basalts assimilated from
1105 lunar regolith. American Mineralogist, 101, 1596-1603.
1106 Turrin, B. D., Christiansen, R. L., Clynne, M. A., Champion, D. E., Gerstel, W. J.,
1107 Patrick Muffler, L., and Trimble, D. A. (1998) Age of Lassen Peak, California,
1108 and implications for the ages of late Pleistocene glaciations in the southern
1109 Cascade Range. Geological Society of America Bulletin, 110, 7, 931-945.
1110 Underwood, S., Feeley, T., and Clynne, M. (2012) Hydrogen isotope investigation of
1111 amphibole and biotite phenocrysts in silicic magmas erupted at Lassen Volcanic
1112 Center, California. Journal of volcanology and geothermal research, 227, 32-49.

1113 Underwood, S., Feeley, T., and Clynne, M. (2013) Hydrogen isotope investigation of
1114 amphibole and glass in dacite magmas erupted in 1980–1986 and 2005 at Mount
1115 St. Helens, Washington. Journal of Petrology, 54, 6, 1047-1070.
1116 Uvarova, Y., Sokolova, E., Hawthorne, F., McCammon, C., Kazansky, V., and Lobanov,
1117 K. (2007) Amphiboles from the Kola Superdeep Borehole: $Fe^{3+}$ contents from
1118 crystal-chemical analysis and Mössbauer spectroscopy. Mineralogical Magazine,
1119 71, 6, 651-669.
1120 Vandenberghe, R. E., & De Grave, E. (2013) Application of Mössbauer spectroscopy in
1121 Earth Sciences. In: Mössbauer Spectroscopy (pp. 91-185). Springer, Berlin,
1122 Heidelberg.
1123 Vennemann, T. W., and O'Neil, J. R. (1996) Hydrogen isotope exchange reactions
1124 between hydrous minerals and molecular hydrogen: I. A new approach for the
1125 determination of hydrogen isotope fractionation at moderate temperatures.
1126 Geochimica et Cosmochimica Acta, 60, 13, 2437-2451.
1127 Walowski, K. J., Wallace, P. J., Hauri, E., Wada, I., and Clynne, M. A. (2015) Slab
1128 melting beneath the Cascade Arc driven by dehydration of altered oceanic
1129 peridotite. Nature Geoscience, 8, 404-408.
1130 Wilson, A. D. (1960) The micro-determination of ferrous iron in silicate minerals by a
1131 volumetric and a colorimetric method. Analyst, 85, 823-827.
1132 Zou, B., and Ma, C. (2020) Crystal mush rejuvenation induced by heat and water
1133 transfer: Evidence from amphibole analyses in the Jialuhe Composite Pluton, East
1134 Kunlun Orogen, northern Tibet Plateau. Lithos, 376, 105722.
1135

## List of Figure captions

**Figure 1.** Schematic illustration of the single-crystal orientations relative to the x-ray propagation and polarization directions. Note these are transmission measurements. The canting angle describes the orientation of the crystal axes with respect to the x-ray propagation direction and is 0° in orientation 1 and 3 and 90° in orientation 2 (see text for explanation and fit of canting angle). These directions are not always along principle crystallographic directions. The exact propagation direction is given in Supplementary Table 1 for each grain.

**Figure 2.** Schematic illustration of the nuclear forward scattering setups at sector 3, Advanced Photon Source, Argonne National Laboratory. The sample is rotated along its crystallographic axes to collect time-domain synchrotron-Mössbauer spectra along different orientations (Fig. 1). In setup B, a Mössbauer drive can be inserted before slit 1 to allow for data collection in the energy domain. Setup B allows to collect a longer delay-time spectra compared to setup A and with a higher incident beam power density (A: $1.7 \times 10^7$ photon/s/μm$^2$ *vs* B: $1.0 \times 10^{10}$ ph/s/μm$^2$). Both setups use a high-heat load monochromator in station 3ID-A as indicated in the schematic.

**Figure 3. (a)** Nomenclature of amphiboles following Hawthorne et al. (2012). Ferric iron content determined by synchrotron Mössbauer spectroscopy; **(b)** Water content (wt%) and δD (in ‰ relative to SMOW) of amphiboles determined by secondary-ion mass spectrometry. The yellow lines show a Rayleigh fractionation model indicating the trend caused by $H_2$ release (dehydrogenation) in amphiboles (fractionations of -100‰ and -

80‰). The starting composition of the model (yellow square) has 1.65 wt% $H_2O$ and a δD composition of -86 ‰. The range of arc melt inclusions is from Shaw et al. (2008) and Walowski et al. (2015). See text for details. Errors are smaller than the symbol size if not shown.

**Figure 4. Left:** Backscatter electron images of grains showing electron microprobe and secondary-ion mass spectrometry analysis spots and the areas where SMS spectra were collected. **Right:** Variation in major element oxides determined by EMPA along transects through the grains. For uncertainties of EMPA analysis see text. **(a)** MC18-2; **(b)** LF02-042; **(c)** SH315-4; **(d)** PH13A A1; analyzed points are connected by lines for clarity; **(e)** PH13A A2.

**Figure 5.** Synchrotron Mössbauer spectra of grain MC18-2: **(a)** 24-bunch mode spectra of orientation 1 and 2 collected with a Cu aperture; **(b)** 24-bunch mode spectra of orientation 1 collected without a Cu aperture; (c) hybrid mode time domain spectrum collected for 1 hour for orientation 1; **(d)** hybrid mode energy domain spectrum collected for 12 hours for orientation 1; (e) calculated energy domain data using the best fit values from (d). Corresponding best fits are shown with $\chi^2$ for each fit and resulting $Fe^{3+}/Fe^{T}$ ratios. The calculated breakdown of the site doublets and their sum for the energy spectrum uses the best-fit hyperfine parameters, transmission integral, and a linear polarized x-ray source.

**Figure 6.** Synchrotron Mössbauer spectra of grain LF02-042: **(a)**, **(b)**, and **(c)** 24-bunch mode spectra of orientation 1, 2, and 3; **(d)** hybrid mode time domain spectrum collected for 1 hour for orientation 1; **(e)** hybrid mode time domain spectrum collected for 12 hours for orientation 1. Corresponding best fits are shown with $\chi^2$ for each fit and resulting $Fe^{3+}/Fe^{T}$ ratios.

**Figure 7.** Synchrotron Mössbauer spectra of grain SH315-4: **(a)** and **(b)** 24-bunch mode spectra of orientation 1 and 2 collected with a Cu aperture; **(c)** 24-bunch mode spectra of spot 3 for orientation 1 (see Fig. 4c for location on the grain); **(d)** hybrid mode time domain spectrum collected for 1 hour for orientation 1; **(e)** hybrid mode energy domain spectrum collected for 12 hours for orientation 1; (f) calculated energy domain data using the best fit values from (e). Corresponding best fits are shown with $\chi^2$ for each fit and resulting $Fe^{3+}/Fe^{T}$ ratios. The calculated breakdown of the site doublets and their sum for the energy spectrum uses the best-fit hyperfine parameters, transmission integral, and a linear polarized x-ray source.

**Figure 8.** Synchrotron Mössbauer spectra of grain PH13A A2: **(a)** and **(b)** 24-bunch mode spectra of orientation 1 and 2 collected with a Cu aperture; **(c)** 24-bunch mode spectra of orientation 1; **(d)** and **(e)** hybrid mode time domain spectrum collected for 1 hour for orientation 1 and 2; **(f)** 24-bunch mode spectra of orientation 3. Corresponding best fits are shown with $\chi^2$ for each fit and resulting $Fe^{3+}/Fe^{T}$ ratios.

**Figure 9.** Synchrotron Mössbauer spectra of grain PH13A A1: **(a)**, **(b)**, and **(c)** 24-bunch mode spectra of orientation 1, 2, and 3; **(d)** and **(e)** calculated energy domain data using the best fit values from (a) and (b); (**f)** hybrid mode time domain spectrum collected for 1 hour for orientation 1. Corresponding best fits are shown with $\chi^2$ for each fit and resulting $Fe^{3+}/Fe^{T}$ ratios. The calculated breakdown of the site doublets and their sum for the expected energy spectra of orientations 1 and 2 uses the best-fit hyperfine parameters, accounts for the transmission integral and the linear polarized nature of the x-rays, and considers a pristine radioactive source width (1 gamma).

**Figure 10.** Isomer shift (mm/s) relative to α-iron (corrected for isomer shift between the stainless steel foils and α-iron) versus quadrupole splitting (mm/s) for (a) ferrous M(1); (b) ferrous M(2); (c) ferrous M(3); (d) ferric M(2); and (e) ferric M(3). The grey circles are hyperfine parameters from published conventional Mössbauer studies on amphiboles (data and references in Supplementary Table 4). The grey boxes in each panel show the range of hyperfine parameters for each site as assigned by conventional Mössbauer studies. The dashed box in B also shows the range in hyperfine parameters for the ferrous M(4) site. Note that literature data are from all amphibole subgroups, not just calcic amphiboles. Uncertainties for the quadropole splitting and isomer shift determined in this study for Mössbauer sites with weight fractions that are >0.1 are given in Supplementary Table 1 and shown as vertical and horizontal bars. Uncertainty is not shown if smaller than the symbol size.

**Figure 11.** Variations of quadrupole splitting as a function of major element composition, oxo-component, and site occupation: **(a)** and **(b)** site weight of $Fe^{2+}$ at M(2) versus quadrupole splitting of $Fe^{2+}$ at the M(1) and M(3) site (mm/s); **(c)** Mg (apfu) versus quadrupole splitting on the $Fe^{3+}$ M(2) site (mm/s); **(d)** oxo-component (apfu) versus quadrupole splitting of $Fe^{2+}$ at the M(1) (mm/s). Uncertainties for the quadropole splitting are given in Supplementary Table 1.

**Figure 12.** Different mechanisms of ferric iron and oxo-component accommodation in the amphibole structure. Ferric iron determined by synchrotron Mössbauer spectroscopy from area on the grain where major element composition and water content was also determined. The oxo-component was calculated from water contents determined by secondary-ion mass spectrometry. In addition, literature data is shown (Supplementary Table 6 lists the data, references, and the various methods used to determine major element compositions, $Fe^{3+}/Fe^{T}$ ratios, and water content). Mantle-derived amphiboles include ultramafic associations and megacrysts from basaltic lavas; crustal-derived igneous amphiboles encompass amphiboles derived from plutonic and volcanic lithologies; metamorphic amphiboles encompass various metamorphic facies and lithological compositions. Amphibole formula calculations after Locock (2014). **(a)** oxo-component (apfu) versus ferric iron (apfu); **(b)** oxo-component (apfu) versus titanium on the C-site (apfu); **(c)** aluminum on the C-site (apfu) versus ferric iron (apfu); **(d)** A-site vacancy (apfu) versus ferric iron (apfu). Error bar is smaller then the symbol size if not shown.

This is the peer-reviewed, final accepted version for American Mineralogist, published by the Mineralogical Society of America.
The published version is subject to change. Cite as Authors (Year) Title. American Mineralogist, in press.
DOI: https://doi.org/10.2138/am-2022-8115. http://www.minsocam.org/

# Figure 1

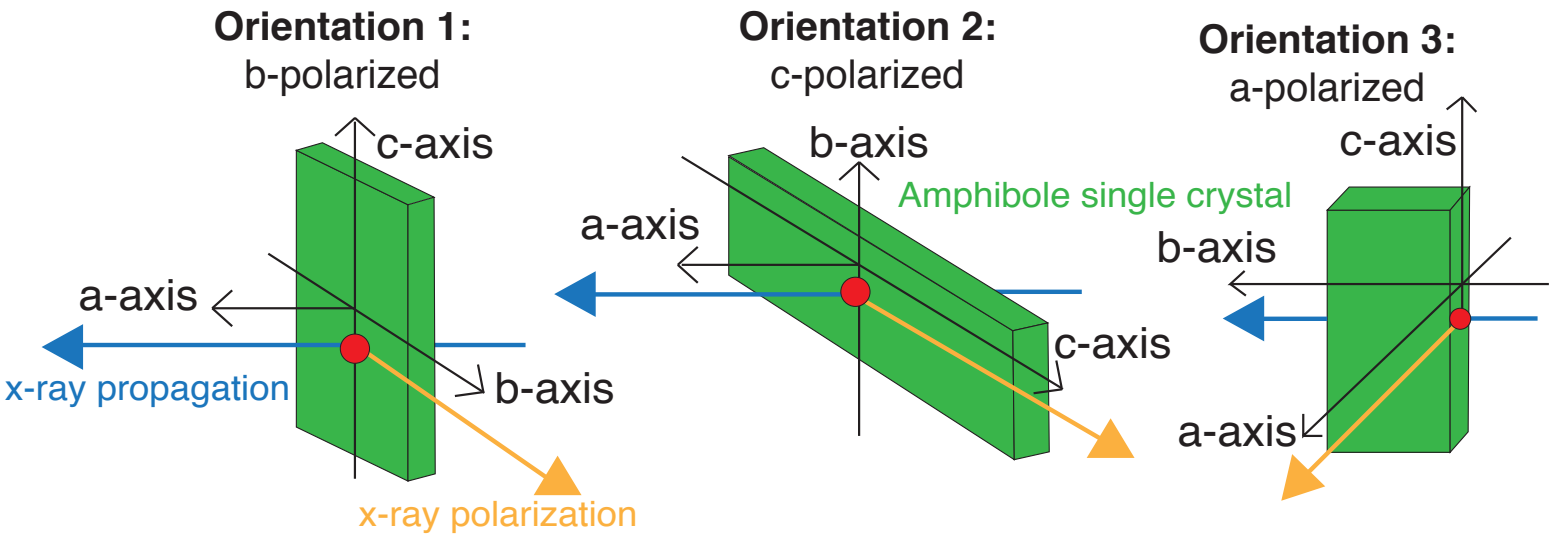

This is the peer-reviewed, final accepted version for American Mineralogist, published by the Mineralogical Society of America.
The published version is subject to change. Cite as Authors (Year) Title. American Mineralogist, in press.
DOI: https://doi.org/10.2138/am-2022-8115. http://www.minsocam.org/

# Figure 2

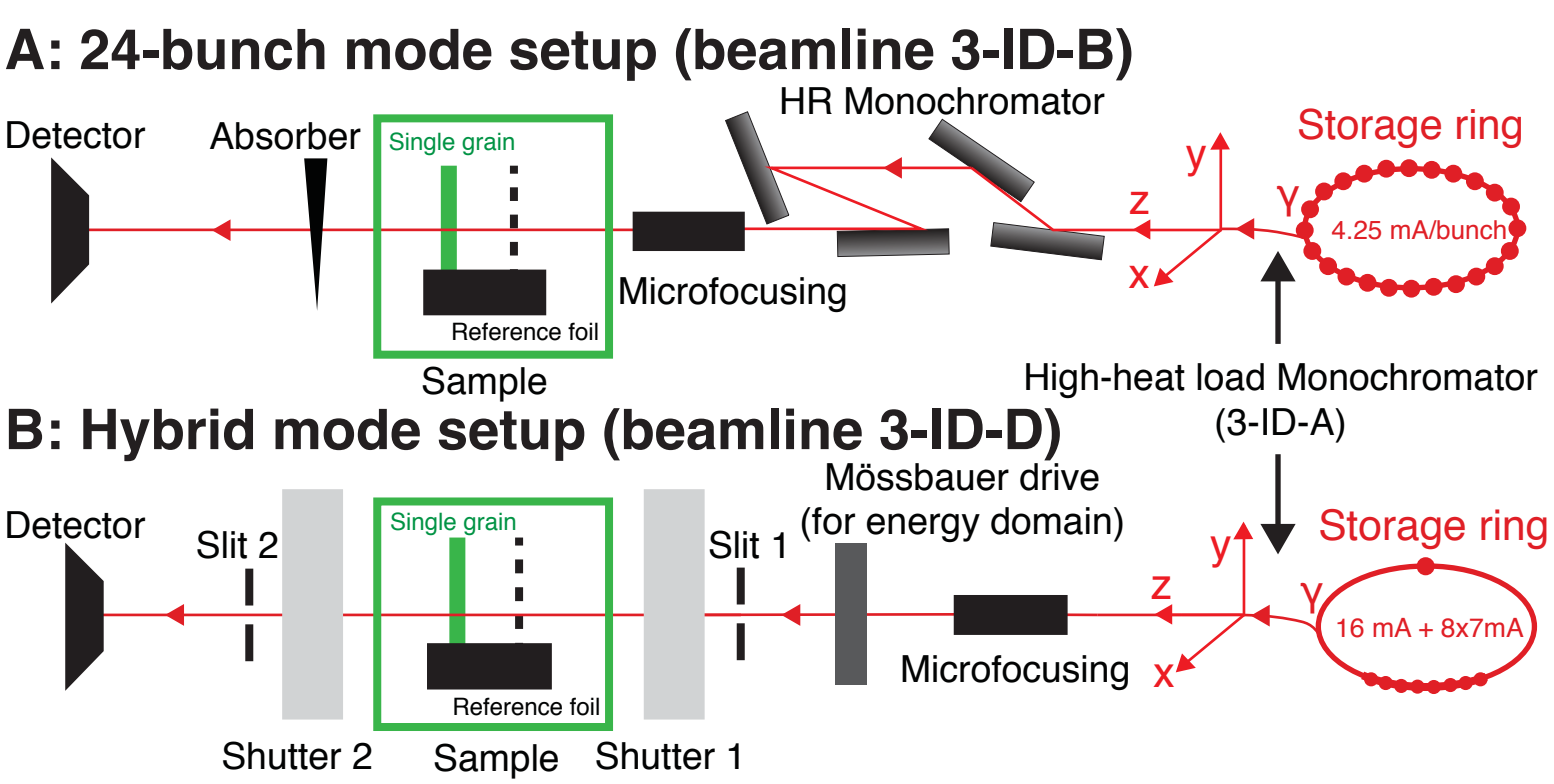

This is the peer-reviewed, final accepted version for American Mineralogist, published by the Mineralogical Society of America.
The published version is subject to change. Cite as Authors (Year) Title. American Mineralogist, in press.
DOI: https://doi.org/10.2138/am-2022-8115. http://www.minsocam.org/

# Figure 3

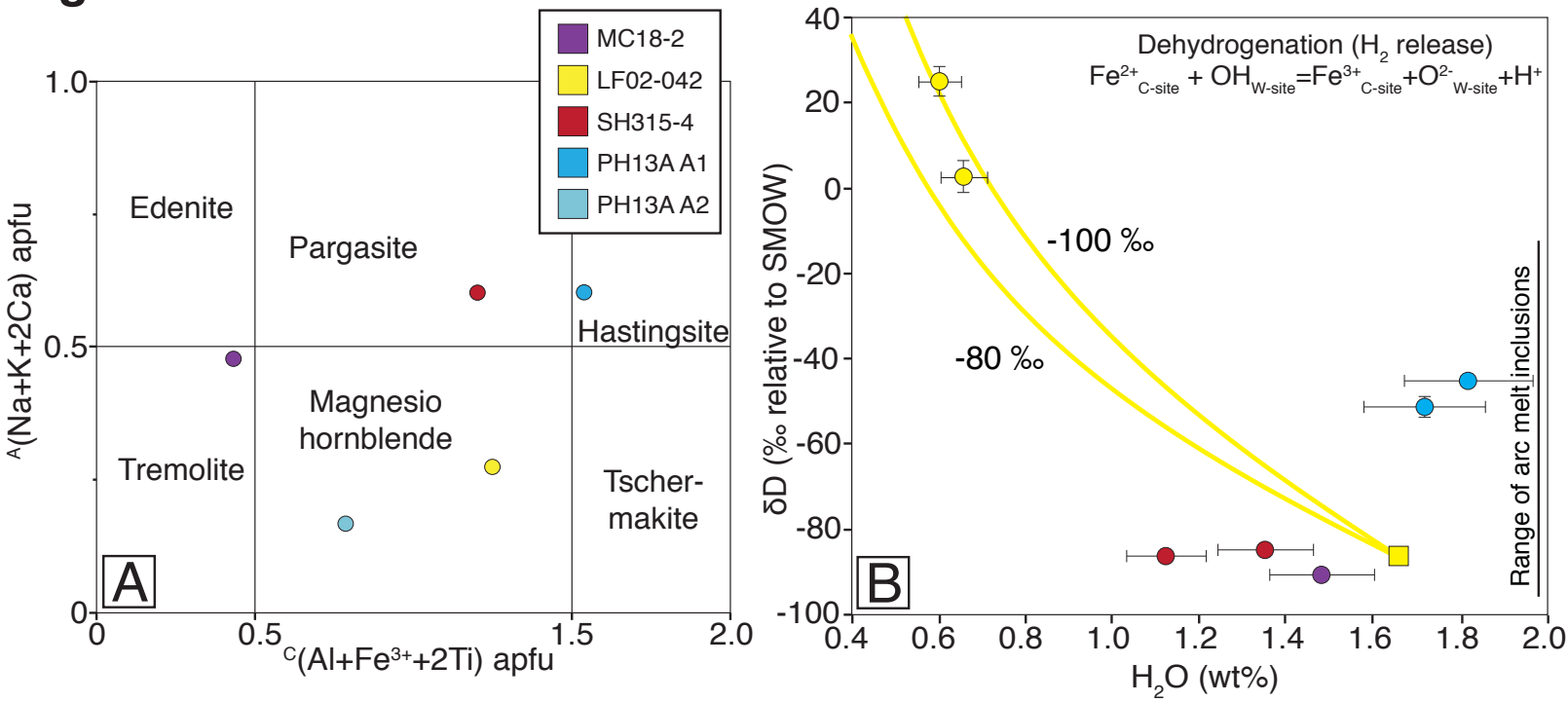

This is the peer-reviewed, final accepted version for American Mineralogist, published by the Mineralogical Society of America.
The published version is subject to change. Cite as Authors (Year) Title. American Mineralogist, in press.
DOI: https://doi.org/10.2138/am-2022-8115. http://www.minsocam.org/

# Figure 4

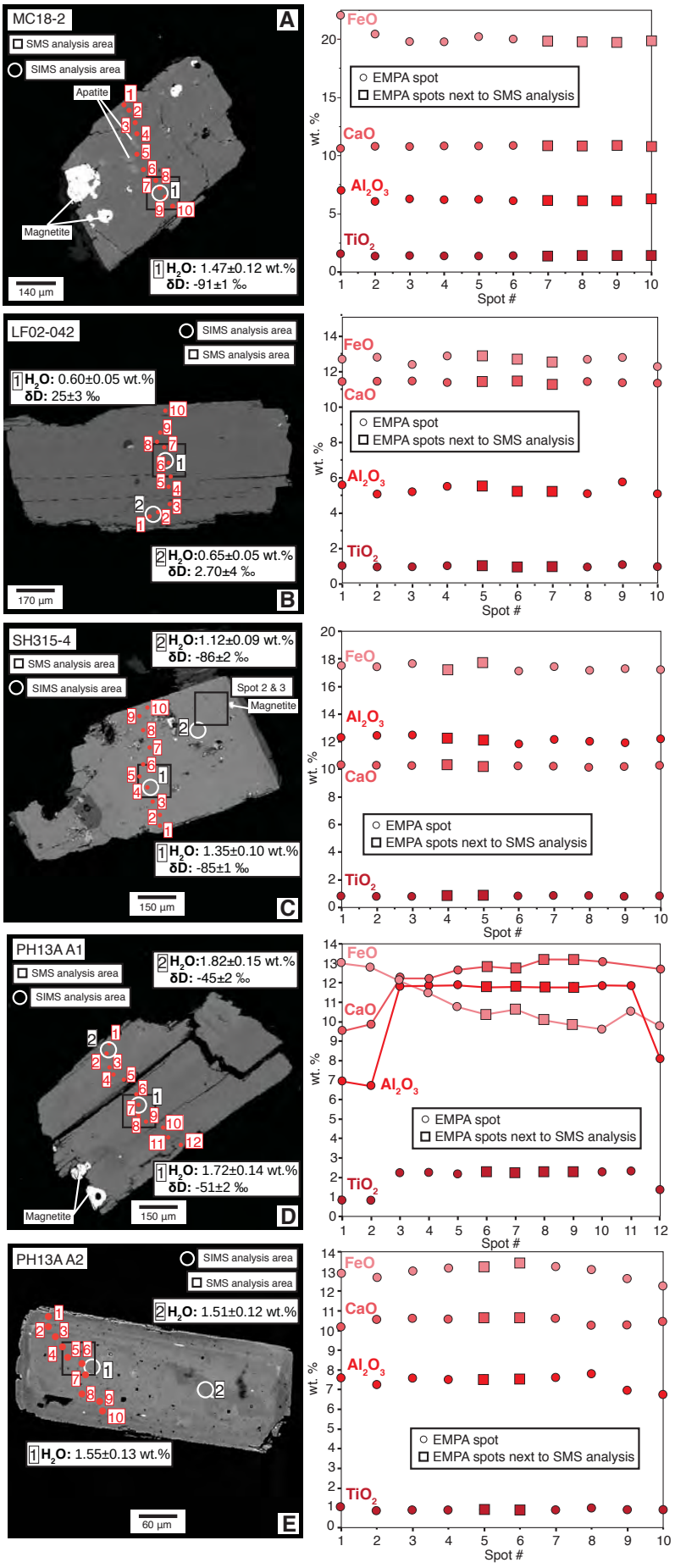

This is the peer-reviewed, final accepted version for American Mineralogist, published by the Mineralogical Society of America.
The published version is subject to change. Cite as Authors (Year) Title. American Mineralogist, in press.
DOI: https://doi.org/10.2138/am-2022-8115. http://www.minsocam.org/

# Figure 5

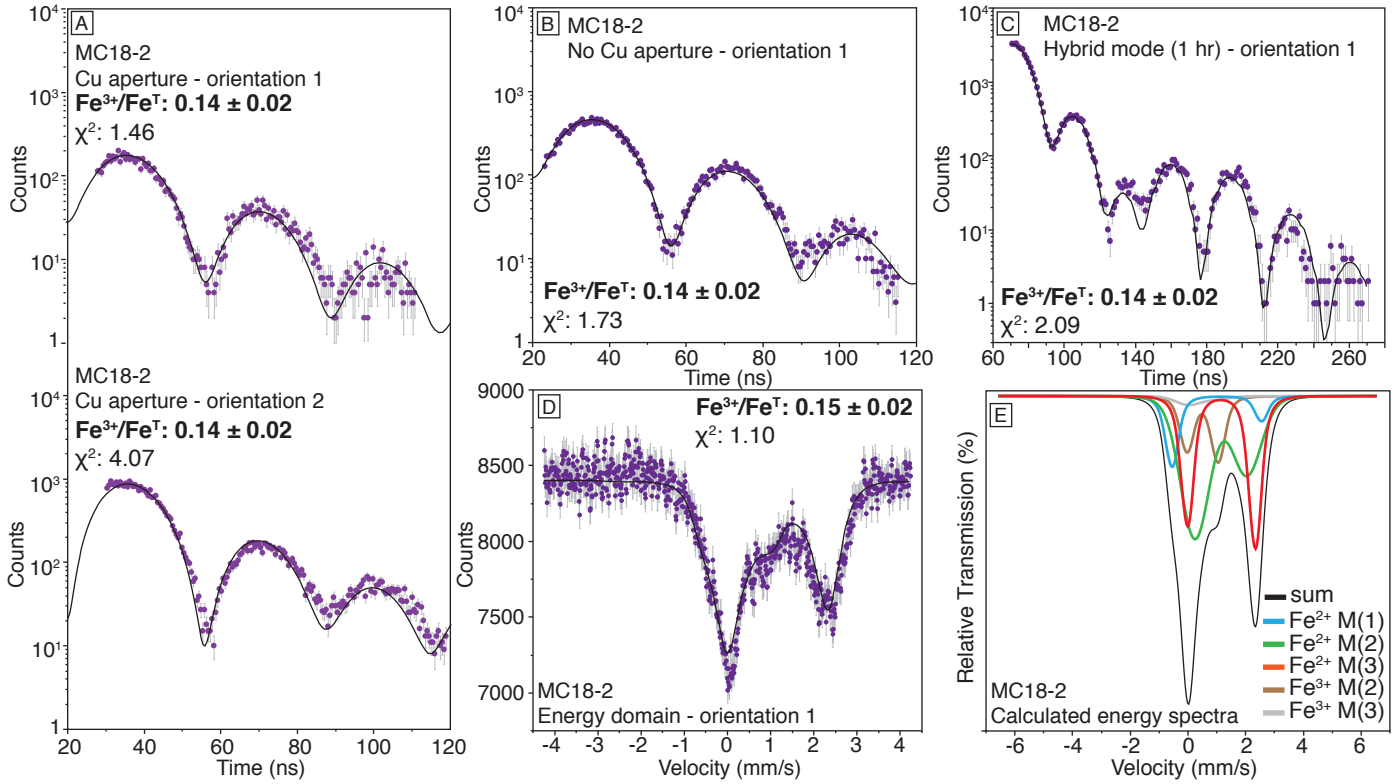

This is the peer-reviewed, final accepted version for American Mineralogist, published by the Mineralogical Society of America.
The published version is subject to change. Cite as Authors (Year) Title. American Mineralogist, in press.
DOI: https://doi.org/10.2138/am-2022-8115. http://www.minsocam.org/

# Figure 6

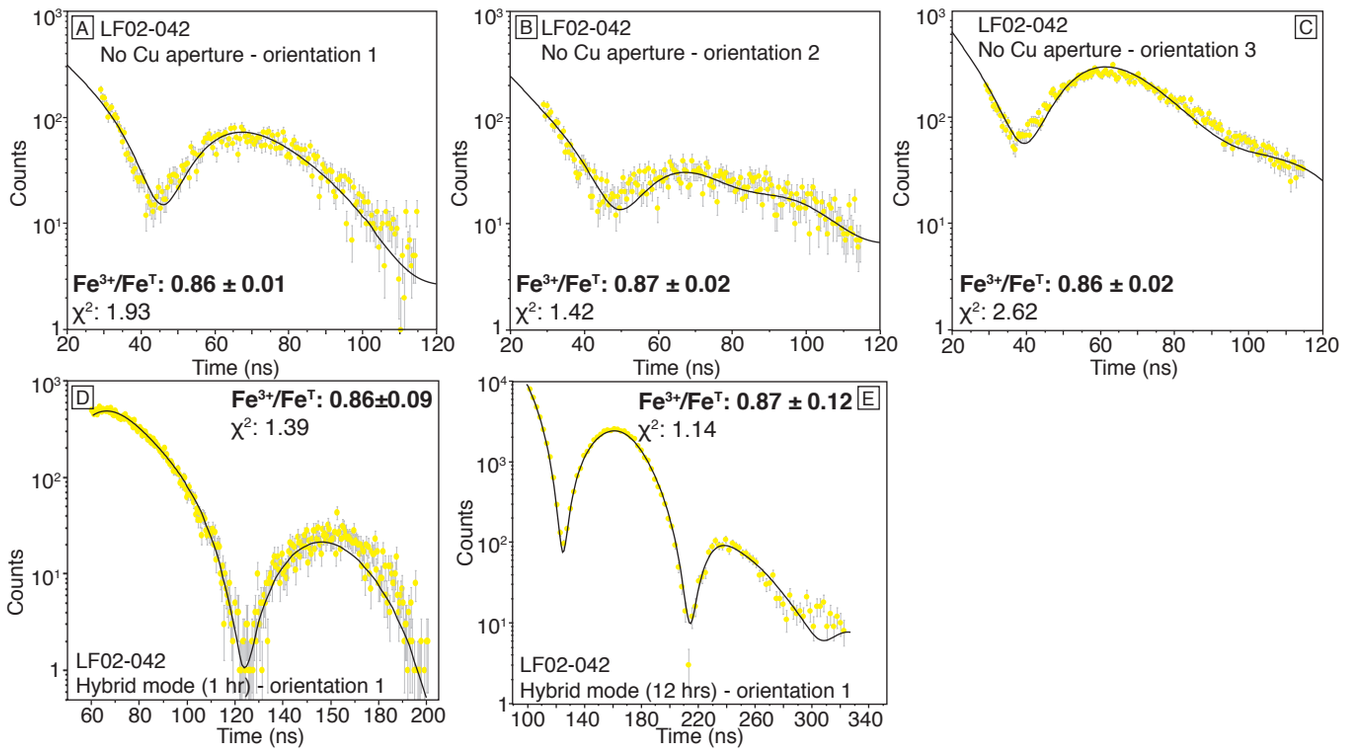

This is the peer-reviewed, final accepted version for American Mineralogist, published by the Mineralogical Society of America.
The published version is subject to change. Cite as Authors (Year) Title. American Mineralogist, in press.
DOI: https://doi.org/10.2138/am-2022-8115. http://www.minsocam.org/

# Figure 7

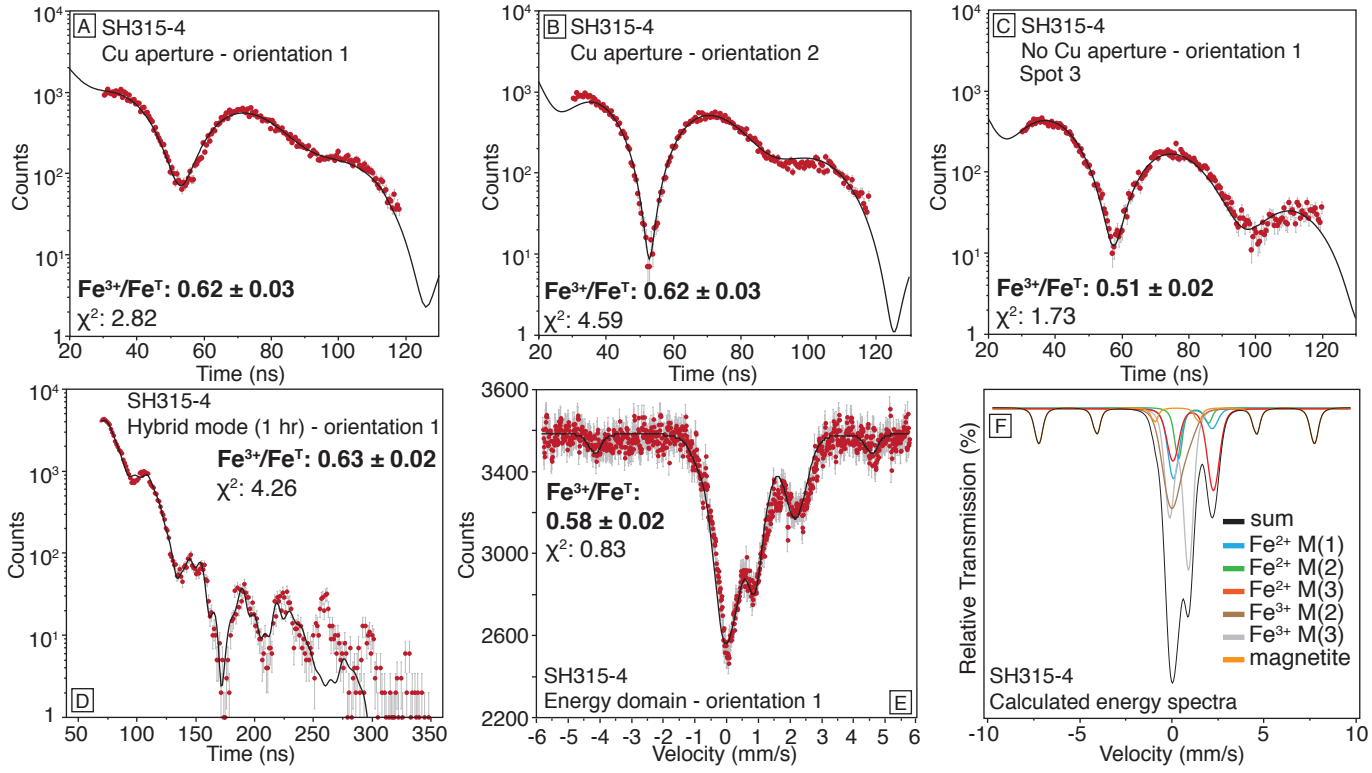

This is the peer-reviewed, final accepted version for American Mineralogist, published by the Mineralogical Society of America.
The published version is subject to change. Cite as Authors (Year) Title. American Mineralogist, in press.
DOI: https://doi.org/10.2138/am-2022-8115. http://www.minsocam.org/

# Figure 8

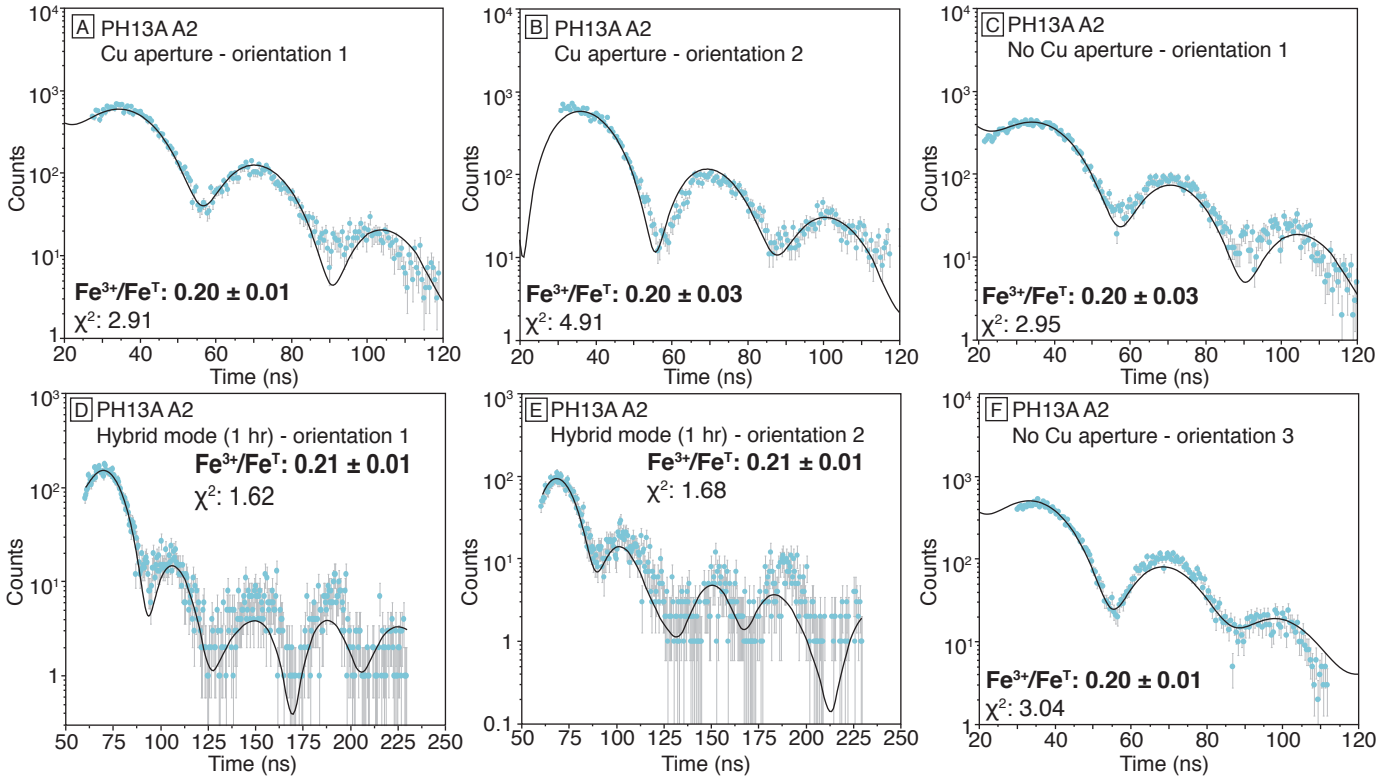

This is the peer-reviewed, final accepted version for American Mineralogist, published by the Mineralogical Society of America.
The published version is subject to change. Cite as Authors (Year) Title. American Mineralogist, in press.
DOI: https://doi.org/10.2138/am-2022-8115. http://www.minsocam.org/

# Figure 9

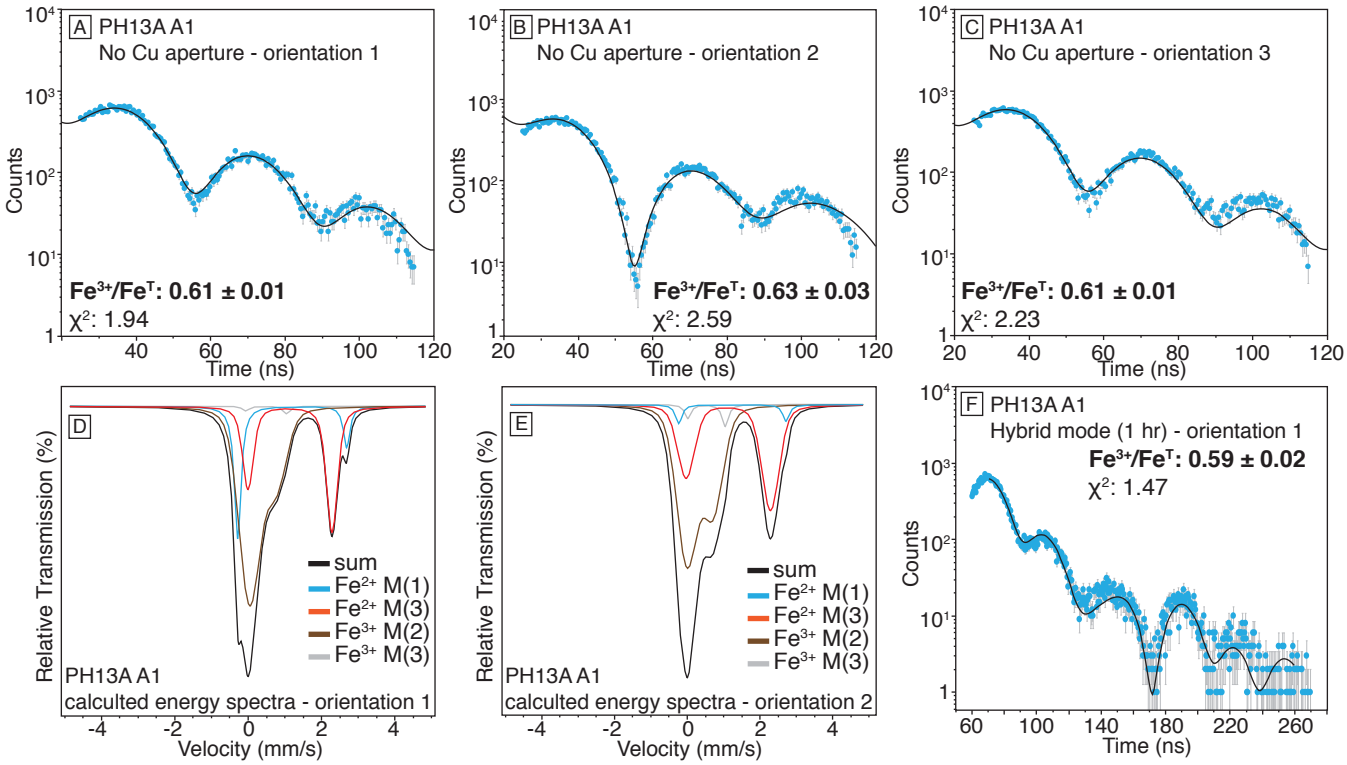

This is the peer-reviewed, final accepted version for American Mineralogist, published by the Mineralogical Society of America.
The published version is subject to change. Cite as Authors (Year) Title. American Mineralogist, in press.
DOI: https://doi.org/10.2138/am-2022-8115. http://www.minsocam.org/

# Figure 10

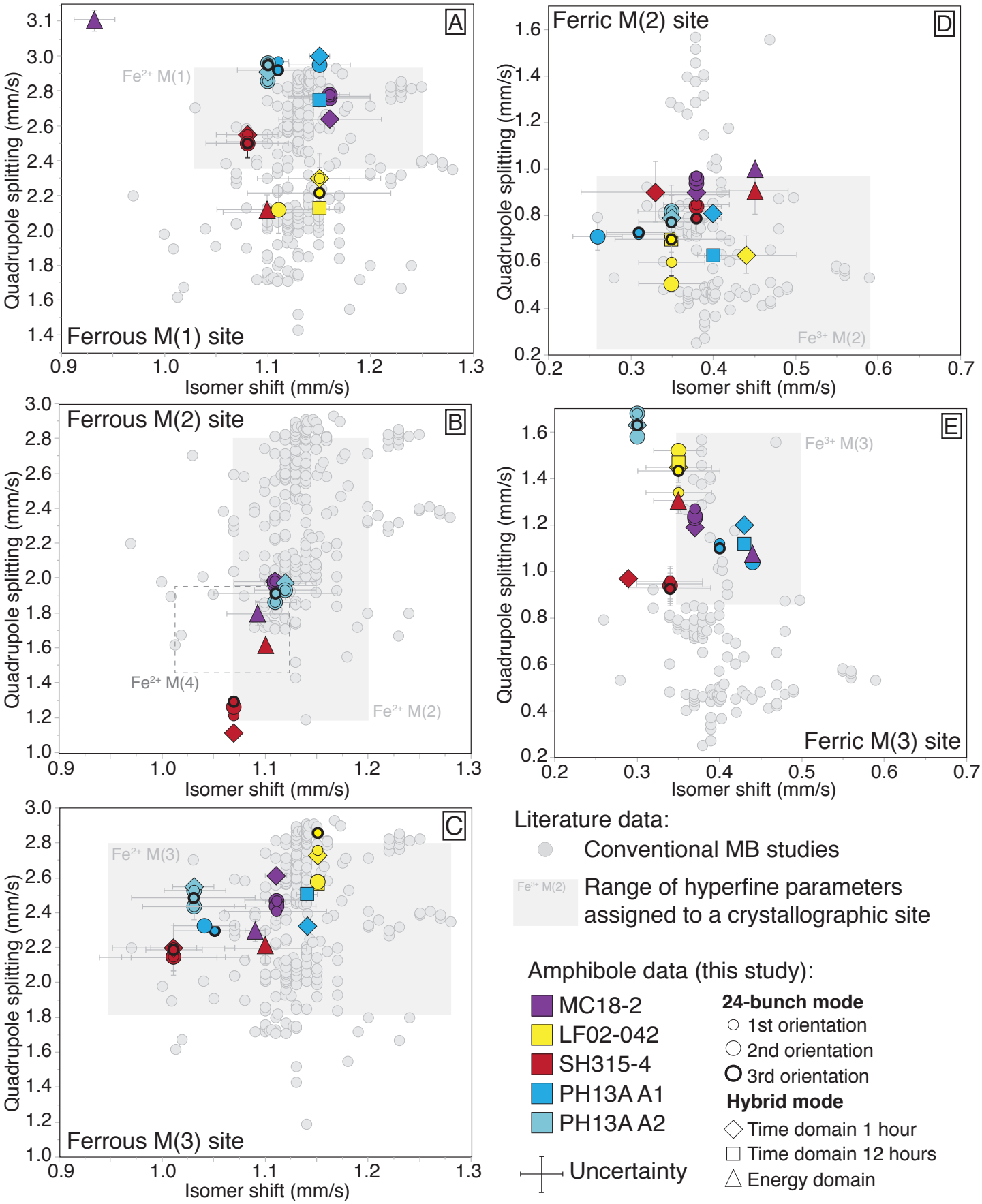

# Figure 11

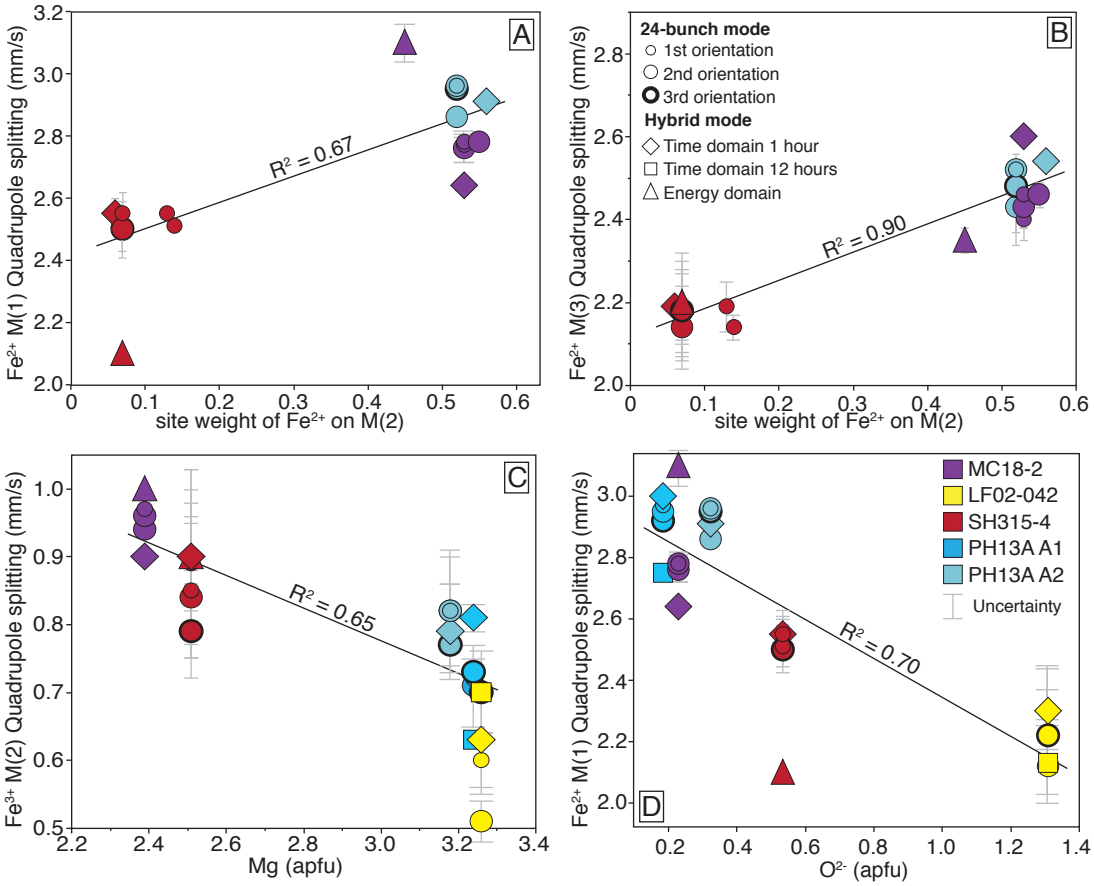

This is the peer-reviewed, final accepted version for American Mineralogist, published by the Mineralogical Society of America.
The published version is subject to change. Cite as Authors (Year) Title. American Mineralogist, in press.
DOI: https://doi.org/10.2138/am-2022-8115. http://www.minsocam.org/

# Figure 12

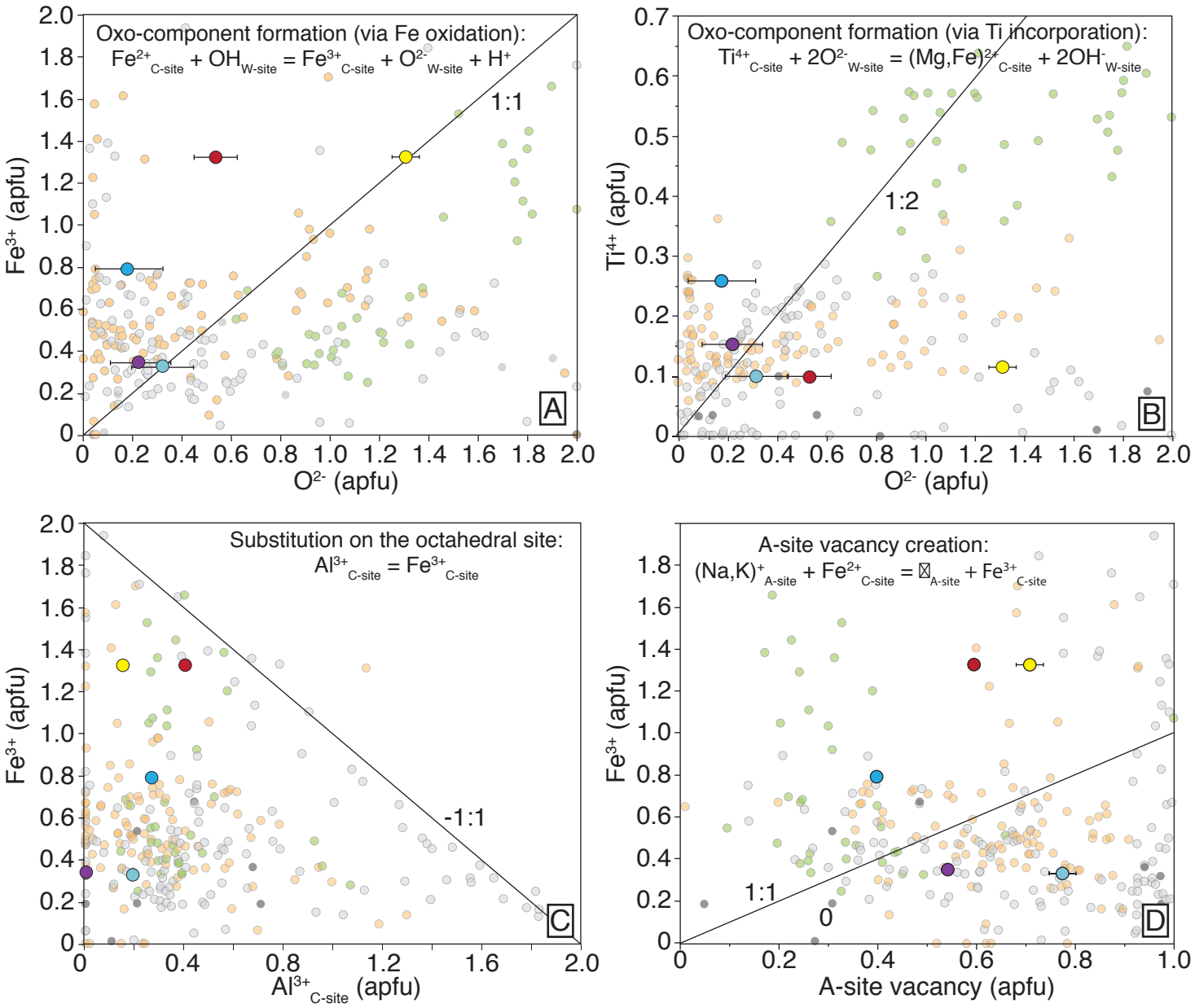


Amphibole data (this study):
- MC18-2
- LF02-042
- SH315-4
- PH13A A1
- PH13A A2

Literature data:
- mantle-derived amphiboles
- crustal-derived igneous amphiboles
- metamorphic amphiboles
- no group affinity